Published April 11, 2019

Increased Bias in Evapotranspiration Modeling Due to Weather and Vegetation Indices Data Sources

Ramesh Dhungel,* Robert Aiken, Paul D. Colaizzi, Xiaomao Lin, R. Louis Baumhardt, Steven R. Evett, David K. Brauer, Gary W. Marek, and Dan O'Brien

ABSTRACT

Complex interactions among meteorological data and vegetation indices are incompletely understood in relation to evapotranspiration (*ET*) calculations for larger spatial domains with higher spatial and temporal resolution. Objectives of this study were to evaluate contributions of inputs to uncertainty in *ET* calculations and to enhance understanding of interactions among weather data, vegetative indices, and resistances utilized in biophysical *ET* model. We evaluated individual and combined effects of weather variables and vegetation indices using BAITSSS (Backward-Averaged Iterative Two-Source Surface temperature and energy balance Solution). Local weather station (LWS) data at a lysimeter site were obtained for irrigated corn (Zea mays L.) during the growing season (May to September, 2016) at Bushland, Texas. Gridded meteorological data were obtained from North American Land Data Assimilation System (NLDAS) (~ 12.5 km) and remotely-sensed vegetation indices (Landsat 30 m). Standard weather station (SWS) data were obtained from a grass reference near lysimeter site. The r^2 and RMSE of *ET* simulated using LWS data and measured vegetation indices were 0.90 and 0.85 mm for daily *ET*, and 0.90 and 0.10 mm, for hourly *ET*, compared to lysimeter *ET* (less than 4% cumulative error). However, r^2 and RMSE were 0.74 and 1.64 mm for daily *ET*, and 0.81 and 0.14 mm for hourly *ET* using gridded data, with positive bias (~ 25% from NLDAS data). Simulated *ET* from SWS data exhibited similar behavior to gridded data with increased *ET* up to 21%. Results quantify difficulties in *ET* modeling using commonly available and widely adopted data sources.

Core Ideas

- Increased bias in ET due to various data sources where generally utilized standard weather data poses similar biases.
- Increased understanding of the complex relationship among the various weather input and vegetation indices.
- Results showed local weather station data closely represented site condition indicating the difficulties and challenges in ET modeling using other commonly available and widely adopted data sources.

Published in Agron. J. 111:1407–1424 (2019)
doi:10.2134/agronj2018.10.0636
Available freely online through the author-supported open access option

Surface energy balance algorithms require accurate meteorological data and vegetation indices to generate accurate water and energy fluxes including evapotranspiration (ET) (Kotlarski et al., 2005; Allen et al., 2011b; Wang et al., 2015). High-resolution accurate ET maps could be vital to managing water, especially in agricultural landscapes that experience water scarcity (Gowda et al., 2008; Anderson et al., 2012; Khanal et al., 2017; Kiptala et al., 2018; Petropoulos et al., 2018). Various models, types of weather data, and vegetation indices from different data sources are frequently used to compute large-scale high resolution evapotranspiration (ET) (Courault et al., 2005). Landscape-scale ecological modeling is hindered by the lack of suitable data as well as scale mismatch (Root and Schneider, 2002; Abatzoglou, 2013), posing challenges to model parameterization and specification of model inputs (Renard et al., 2010).

In this study, biophysical ET algorithm; BAITSSS (Backward-Averaged Iterative Two-Source Surface temperature and energy balance Solution) (Dhungel et al., 2016b) was utilized to simulate ET in a point and a gridded scale at an advective environment of Bushland, Texas. BAITSSS was developed to fulfill the future demand of more accurate and detailed modeling approach for surface energy fluxes (Dhungel et al., 2016b, 2018) as pointed out by Woolway et al. (2015). Evaluations of model performance with alternative sources of meteorological data in various environments and for different vegetation types can contribute to the understanding of model behavior and uncertainty. BAITSSS utilizes gridded data primarily from the North American Land Data Assimilation System; NLDAS; (Mitchell et al., 2004) and remotely sensed vegetation indices (Leaf area index; *LAI*) and Normalized difference vegetation index (*NDVI*) primarily from Landsat: 30 m spatial resolution). Comprehensive weather data provided by NLDAS included 1/8° latitude/longitude resolution over a domain that covers the continental United States, part of Canada, and part of Mexico (125° W –67° W, 25° N –53° N) in

R. Dhungel, and X. Lin, Dep. of Agronomy, Kansas State Univ., 1712 Claflin St., Manhattan, KS 66506; R. Aiken, and D. O'Brien, Northwest Research-Extension Center, Kansas State Univ., Colby, KS 67701; and P.D. Colaizzi, R.L. Baumhardt, S.R. Evett, D.K. Brauer, and G.W. Marek, USDA-ARS, Conservation and Production Research Laboratory, P. O. Drawer 10, Bushland, TX 79012. Received 2 Oct. 2018. Accepted 29 Jan. 2019. *Corresponding author (rdhungel@ksu.edu).

Abbreviations: area of interest (AOI); Backward-Averaged Iterative Two-Source Surface temperature and energy balance Solution (BAITSSS); day of year (DOY); including evapotranspiration (*ET*); irrigation (I_{rr}); leaf area index (*LAI*); local weather station (LWS); normalized difference vegetation index (*NDVI*); North American Land Data Assimilation System (NLDAS); precipitation (P); relative humidity (*RH*); soil adjusted vegetation index (*SAVI*); Soil and Water Management Research Unit (SWMRU); Standard Weather Station (SWS)

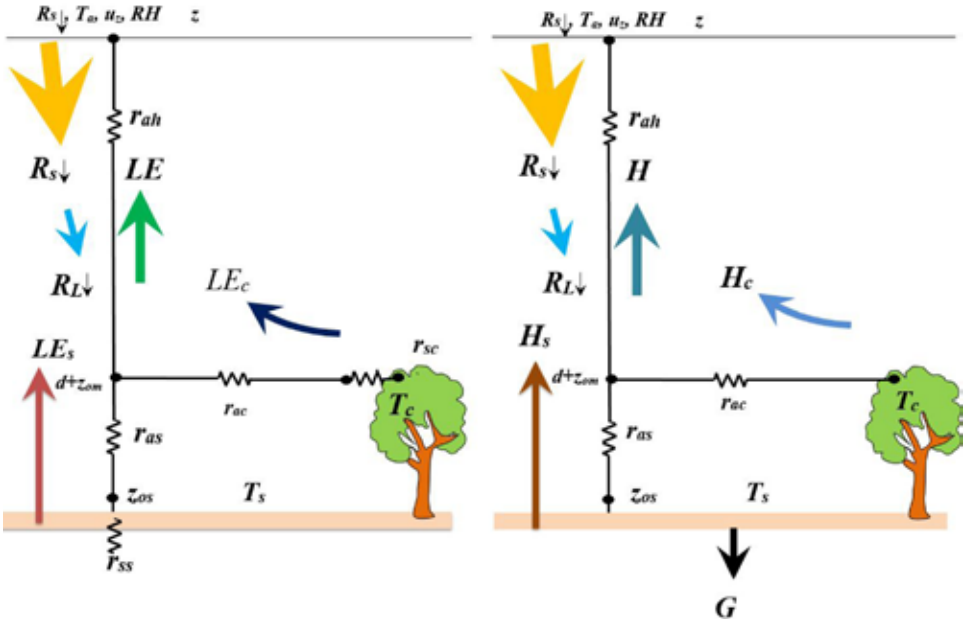

Fig. 1. Modeling scheme for a) latent heat flux (*LE*) and b) sensible heat flux (*H*) of BAITSSS surface energy balance components (Dhungel et al., 2016b).

hourly resolution, beginning in 1979. NLDAS weather data have been used in hydrological and atmospheric research, including *ET* modeling (Mitchell et al., 2004). The point hourly data was acquired from local weather station (LWS) and standard weather station (SWS) in close proximity of study area.

Extent of the uncertainty in these various data sources including remote sensing products (Von Schuckmann et al., 2016) is generally unknown and difficult to be quantified at different scales because of complex interactions among variables in *ET* modeling (Brutsaert, 1982). It is useful to distinguish between model limitations and various biases (Schimel et al., 1997) caused by input data that may not represent the actual weather and vegetation indices in a given field. For instance, the sensitivity of reference *ET* based on the Penman–Monteith equation weather variables [daily air temperature (T_a), wind speed (u_z), relative humidity (RH), and daily sunshine duration ($R_s\downarrow$)] showed wide variation by season and region (Gong et al., 2006; Guo et al., 2017). Likewise, a two-fold increase in potential *ET* was observed in Australian locations using the Penman–Monteith equation, where u_z and RH were the most sensitive variables (Guo et al., 2017). The major objectives of this study were to evaluate the contributions of inputs to uncertainty in *ET* calculation and evaluate the sensitivity in an energy balance model to influences of gridded and local data. This study would provide a unique opportunity to improve the understanding of interactions among weather variables, vegetation indices, and resistances. Our overall goal is to develop python ("Python," 2018), together with GDAL and Numpy libraries based automated operational *ET* model (BAITSSS) utilizing NLDAS weather data and Landsat based vegetation indices at 30 m spatial resolution, hourly scale with known and quantifiable uncertainties.

MATERIALS AND METHODS

BAITSSS Model Overview

Details of the BAITSSS model and equations were shown in Dhungel et al. (2016b) and updated equations in Appendix A. BAITSSS utilizes a physically-based representation of radiative and convective processes affecting heat and water vapor exchange for land and vegetative surfaces. BAITSSS adopts the Jarvis equation (Eq. [A-13]) to compute canopy resistance (r_{sc}) (Kumar et al., 2011) where constant minimum canopy resistance [R_{c_min}; Day of year (DOY) 143 to 250] for irrigated corn was 40 s m^{-1} (Kumar et al., 2011) and increased R_{c_min}, i.e., 150 s m^{-1} thereafter (last 20 d) during the assumed senescence period as per the analysis reported in Dhungel et al. (2018) (in review; identical study based on 15-min LWS data). The scheme of modeling latent heat flux and sensible heat flux based on aerodynamic equations were shown in Fig. 1 with soil (subscript *s*) and canopy (subscript *c*) (Appendix- Eq. [A-1– A-10], Table A-1 shown for all variable symbols).

Data

The simulation period was between 22 May (DOY 143) and 26 September (DOY 270) 2016, corresponding to 12 d after planting to maturity of drought-tolerant corn (Zea mays L. cv. PIO 1151). This simulation interval included a range of environmental conditions with multiple drying and wetting events. BAITSSS was implemented for a single location (point scale; one dimentional) as well as gridded spatial domain (NLDAS weather data and Landsat-based vegetation indices) (Table 1). Effects of alternative input data sources on BAITSSS model performance were analyzed by substituting a 'gridded' input for a measured input, individually and in combinations. These combinations represent the following scenarios; a) all measured (including irrigation (I_{rr}); 15 min to hour), b) fraction of cover (f_c), c) *LAI*, d) precipitation (P), e) specific humidity (q_a), f) $R_s\downarrow$, g) I_{rr}, h) f_c and *LAI*, i) u_z and T_a, j) combined q_a, $R_s\downarrow$, and P, k) combined q_a, $R_s\downarrow$, P, T_a, and u_z (all NLDAS), l) all gridded data (Table 2). Dhungel et al. (2018) discussed the possible effect of advection in *ET* calculation based on LWS data, our implicit assumptions and limitation of this study were all these data sources (LWS, SWS, and gridded data) may be subject to similar effects of regional and local advection.

Table 1. Meteorological data, vegetation indices, and other variables.

Variable	Gridded (NLDAS hourly)	Point (NE lysimeter hourly averaged; LWS)	Point (SWMRU hourly averaged; SWS)
Meteorological data		Measurement height	
Air temperature (T_a)	2 m	2.8 m	2 m
Wind speed (u_z)	10 m	2.8 m	2 m
Specific humidity (q_a)	2 m	–	–
Relative humidity (*RH*)	–	2.8 m	2 m
Incoming solar irradiance ($R_{s\downarrow}$)	Surface	Surface	Surface
Precipitation (*P*)	Surface	Surface	Surface
Surface runoff (S_{run})	Surface	–	–
Vegetation indices		Data sources	
Leaf area index (*LAI*)	Estimated based on Landsat	Measured	Measured
Normalized difference vegetation index (*NDVI*)	Landsat	–	–
Fraction of canopy cover (f_c)	Estimated from *NDVI* using Landsat	Estimated from measured ratio of canopy width to row spacing	Estimated from measured ratio of canopy width to row spacing
Other			
Irrigation (I_{rr})	Simulated	Measured	Measured
Field capacity (θ_{fc}) and wilting point (θ_{wp})	Gridded data	Point data	Point data

Study Area

The study area was located at the USDA-ARS Conservation and Production Research Laboratory at Bushland, Texas (35° 11′ N, 102° 6′ W, and 1170 m above MSL) with an advective environment. Measurement of *ET* was by a monolithic weighing lysimeter (NE Lysimeter, Fig. 2) located in the center of a 450 m × 439 m field. The lysimeter surface was 3 m by 3 m (containing four crop rows) and 2.4 m deep. Detailed information about the lysimeter (Evett et al., 2016), corresponding weather data, and vegetation indices are shown in Table 1 and described in Fig. 2, 3, 4, 5, and 6. A small area of interest (AOI) for Landsat imagery was carefully selected, avoiding Landsat 7 stripe effects for the NE lysimeter site (Fig. 2). The NLDAS data being 1/8° latitude/longitude resolution (~ 12.5 km), the AOI is represented by a single pixel of NLDAS.

Initial Soil Moisture and irrigation

A relatively dry profile (θ_{sur} = 0.05 m^3 m^{-3}; soil volumetric water content) was adopted for the surface, evaporative layer (100 mm) at the start of the simulation. However, Dhungel et al. (2018) utilized θ_{sur} = 0.15 m^3 m^{-3} based on relative soil sensor information, where *ET* was overestimated for the first 2 d i.e., DOY 143 and 144, which probably may be because of the adopted simplified evaporation model in BAITSSS (Eq. [A-21]). Further evaluation is needed in this regard if this behavior persists systematically. We adopted depth averaged soil water content at root zone (θ_{root}) which was 0.32 m^3 m^{-3} based on repeated neutron probe observations at the start of the simulation. Irrigation (I_{rr}) was applied through controlled subsurface drip (SSD) lines and measured throughout the study; no I_{rr} was applied at the upper soil surface (top 100 mm) in the field, preventing evaporation at the soil surface from irrigation. The I_{rr} application target amounts were 25 mm in the lysimeter field (Fig. 5b).

In I_{rr} sub-model in BAITSSS, $I_{rr\,(i)}$ was simulated and applied when θ_{root} was below a given threshold moisture content (θ_t; *i* is time step, Eq. [1]) (Dhungel et al., 2016b). To mimic the behavior of actual measured I_{rr} in the field (~ 25 mm target application and SSD), rooting depth (d_{root}) and management allowable depletion (*MAD*) was adjusted and I_{rr} was applied only in the root zone. We utilized *MAD* of 0.5 throughout the simulation process. The rest of the variables [i.e., soil moisture at field capacity (θ_{fc}) and wilting point (θ_{wp})] were defined from observed field measurements.

$$I_{rr(i)} = \begin{cases} (\theta_{fc} - \theta_{root(i)})\, d_{root} & if\ \theta_{root(i)} < \theta_t \\ 0 & if\ \theta_{root(i)} \geq \theta_t \end{cases} \quad [1]$$

Point Scale Data

Micrometeorological and surface temperature measurements were obtained by instruments deployed on a ~3 m mast located at the north edge of the NE lysimeter (referred as local weather station– LWS, Fig. 2a). 15-min weather data were averaged hourly for simulation and comparison. The T_a and *RH* were measured by a sensor assembly contained inside a radiation shield (model Hygroclip, Rotronic Instrument Corp., Hauppauge, New York). The u_z was measured by a sonic anemometer (model WindSonic 2D, Gill Instruments Ltd., Lymington, Hampshire, UK). Directional brightness temperature was measured by a wireless infrared thermometer with a nadir view centered over the crop row (model SPIP-IRT, Dynamax, Inc., Houston, Texas). Incoming shortwave irradiance was measured by a pyranometer (model PSP, Eppley Laboratories, Newport, Rhode Island) at 2.0 m above the surface.

Standard 15-min weather data T_a, $R_{s\downarrow}$, *P*, u_z, and *RH* were obtained from the USDA-ARS Soil and Water Management Research Unit (SWMRU), Bushland, TX (referred as standard weather station- SWS, Fig. 2a). This weather station was located at a grass reference site ~250 m east of the lysimeter, where ~1 ha of fescue was well-watered by subsurface drip irrigation and maintained at ~0.12 m height. Table 1 summarizes measurement conditions from LWS and SWS. The measurement height (z; Fig. 1; Eq. [A-10]) of T_a was 2 m (for heat) and 10 m for u_z (for momentum) for NLDAS gridded data, while z was 2.8 m for both T_a and u_z (heat and momentum, respectively) for LWS, and 2 m for both T_a and u_z for SWS (Table 1). In the single

Table 2. Possible combinations gridded (NLDAS and Landsat) and measured data based on local weather station (LWS).

S.L.†	Scenario	Cumulative *ET* (mm)	Daily				Hourly				% change in cumulative ET with respect to lysimeter
			Slope	Intercept	r^2	RMSE (mm)	Slope	Intercept	r^2	RMSE (mm)	
a	All measured including irrigation (15 min to hour)	723	0.93	0.61	0.90	0.85	1.04	0.00	0.90	0.10	3.73
b	Fraction of canopy cover	726	0.93	0.61	0.90	0.89	1.04	0.00	0.90	0.10	4.16
c	Leaf area index	659	0.83	0.61	0.87	1.03	0.94	0.00	0.87	0.10	–5.45
d	Precipitation	725	0.97	0.39	0.90	0.88	1.06	0.00	0.91	0.10	4.02
e	Specific humidity	760	0.97	0.68	0.89	1.03	1.07	0.01	0.89	0.11	9.04
f	Solar irradiance	773	0.97	0.78	0.89	1.10	1.04	0.02	0.89	0.11	10.90
g	Irrigation	723	0.93	0.61	0.90	0.85	1.04	0.00	0.90	0.10	3.73
h	Fraction of canopy cover and leaf area index	667	0.83	0.70	0.87	1.0	0.95	0.00	0.88	0.10	–4.30
i	Wind speed and air temperature	753	0.95	0.72	0.89	1.02	1.08	0.00	0.89	0.11	8.03
j	Specific humidity, solar irradiance, precipitation	818	1.05	0.67	0.87	1.46	1.08	0.02	0.88	0.12	17.36
k	Specific humidity, solar irradiance, precipitation, air temp, wind speed (all NLDAS)	875	1.05	1.11	0.78	2.06	1.1	0.03	0.83	0.16	25.54
l	All gridded	789	0.91	1.21	0.74	1.64	0.97	0.04	0.81	0.14	13.20

† The letters correspond with letters used in Figures.

location form, field-measured data included weather conditions, *LAI*, and the ratio of canopy width to row spacing used to compute the fraction of canopy cover (f_c); linear interpolation of vegetation indices provided a continuous representation of these field-measured values throughout the season.

Gridded Data

Estimated *LAI* in gridded form was based on soil adjusted vegetation index (*SAVI*) using Landsat (Allen et al., 2012). The *LAI* and *NDVI* (Landsat 7 (LC07) and 8 (LC08); https://earthexplorer.usgs.gov) were estimated using Landsat images (path 31 and row 36) from following dates: a) 23 May 2016 (LC07), b) 8 June 2016 (LC07), c) 16 June 2016 (LC08), d) 2 July 2016 (LC08), e) 10 July 2016 (LC07), f) 26 July 2016 (LC07), g) 27 Aug. 2016 (LC07), h) 4 Sept. 2016 (LC08), i) 20 Sept. 2016 (LC08), and j) 28 Sept. 2016 (LC07) (LAI; Fig. 2a to 2j, respectively). In this study, we utilized a maximum number of available images to evaluate the accuracy of these gridded vegetation indices and to test the validity of linearity between image dates. *NDVI* from Landsat was used to compute gridded f_c. NLDAS data (https://hydro1.gesdisc.eosdis.nasa.gov/data/NLDAS/NLDAS_FORA0125_H.002/) as meteorological forcings were (solar irradiance ($R_{s\downarrow}$), wind speed (u_z), air temperature (T_a), specific humidity (q_a), and precipitation (P) (Table 1). Gridded u_z from NLDAS at 10 m height was converted to 2.8 m for simulation and comparison purpose (Fig. 3d) using identical roughness length of momentum (z_{om}) (Eq. A-11).

Error and Sensitivity Analysis

The predictive accuracy of calculations was evaluated against field measurements (*ET*, surface temperature and R_n) using a linear regression. Performance measures included the coefficient of determination (r^2), root-mean-square error (RMSE), slope and intercept from the regression of simulated against observed, as well as cumulative *ET*. Responses of the BAITSSS model to gridded input parameters were evaluated using two different comparison baselines. In Section 3.2 and 3.3, comparisons of calculated parameters (i.e., $ET_{sim\ (scenario\ 'ith')}$) are against field measurements ($ET_{\text{lysimeter}}$, *IRT*, net radiometer) (Eq. [2a]). However, for sections 3.2 (part of the discussions), 3.4, and 3.5 comparisons are against BAITSSS using measured inputs ($ET_{sim\ (scenario\ 'a')}$; Eq. 2b).

$$\%ET = \frac{ET_{sim\ (scenario\ 'ith')} - ET_{lysimeter}}{ET_{lysimeter}} * 100 \quad [2a]$$

$$\%ET = \frac{ET_{sim\ (scenario\ 'ith')} - ET_{sim\ (scenario\ 'a')}}{ET_{sim\ (scenario\ 'a')}} * 100 \quad [2b]$$

Model sensitivity to input source was evaluated using a dimensionless sensitivity analysis coefficient (Sv_i) for input variables (Saxton, 1975; Gong et al., 2006; Ambas and Baltas, 2012). (Ampas, 2010), in Eq. [3], ∂ET is the change in *ET* corresponding to ∂V_i, the change in the i^{th} variable (selected variables shown in Fig. 11) that is, the partial derivative (∂) of the *ET* dependency transformed into a nondimensional form (Beven, 1979). The symbol 'σ_{Vi}' is the standard deviation of the

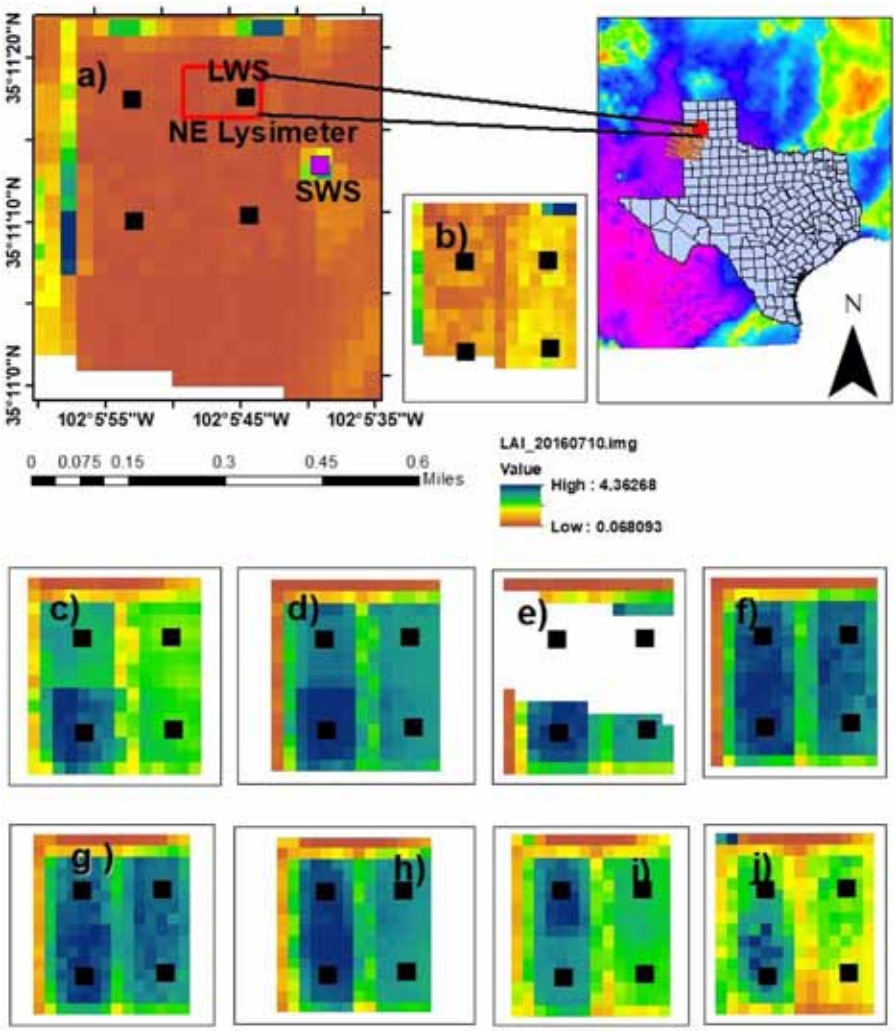

Fig. 2. Study area with lysimeter and *LAI* image based on Landsat path 31 and row 36 (upper left, red border), lysimeter site at various dates with *LAI* images (a to j), incoming solar irradiance from NLDAS (05/09/2016), and State of Texas (upper right).

ith meteorological variable. The change (Δ) in ET represents the difference of a BAITSSS simulation using the gridded form of the ith variable [$ET_{sim\ (scenario\ 'ith')}$] and the simulation using all measured input [$ET_{sim\ (scenario\ 'a')}$]. Daily and seasonal mean sensitivity analysis coefficients were reported.

$$Sv_i = \lim_{\Delta V_i \to 0} \left(\frac{\Delta ET / ET}{\Delta V_i / \sigma_{Vi}} \right) = \frac{\partial ET}{\partial V_i} * \frac{\sigma_{Vi}}{ET} \qquad [3]$$

RESULTS AND DISCUSSION

The analysis of uncertainty in calculated ET begins with comparison of NLDAS and sources of meteorological data with that observed at the lysimeter site (LWS) and followed by comparison of LWS and SWS. Differences in sources of P, I_{rr}, and vegetation indices are then presented. The effects of these differences in inputs and sources on calculated ET, as well as surface temperature and net radiation (R_n), are presented as a set of scenarios. Sensitivities of the BAITSSS model, based on differential weather and canopy input values, are presented. Finally, simulation based on grass-reference weather (SWS) data is related to previous results.

Weather Data and Vegetation Indices

Comparison between Gridded NLDAS and Local Weather Station (LWS) Data

Figure 3 shows an hourly comparison between gridded NLDAS and site measured meteorological data (LWS). As shown in Table 1, the measurement height of measured data was not identical to gridded data, though they are comparable. Because of mismatch on measurement height and coarse resolution of gridded NLDAS data, and possibly other factors (such as roughness lengths and possibly advection), some form of biases are probably expected in these scatterplots. Regression of NLDAS gridded data against LWS data resulted in an RMSE of 113 W m^{-2}, 3.73°C, 0.33 kPa, and 1.37 m s^{-1}, respectively, for $R_{s\downarrow}$, T_a, e_a, and u_z. Compared to other variables, $R_{s\downarrow}$ showed a large bias (Fig. 3a) where Luo et al. (2003) also found a similar bias (RMSD 130 W m^{-2}) between the ground based weather stations and NLDAS at the southern Great Plains. This overestimation of $R_{s\downarrow}$ in NLDAS data was possibly due to the lack of capturing cloud cover (Luo et al., 2003). Gridded T_a tended to have a slightly positive bias (Fig. 3b). The q_a in terms of e_a tended to have a negative bias when compared to measured data (Fig. 3c). Out of all NLDAS data, modeled T_a matched measurements the most (r^2 = 0.89 and low RMSE) (Lewis et al.,

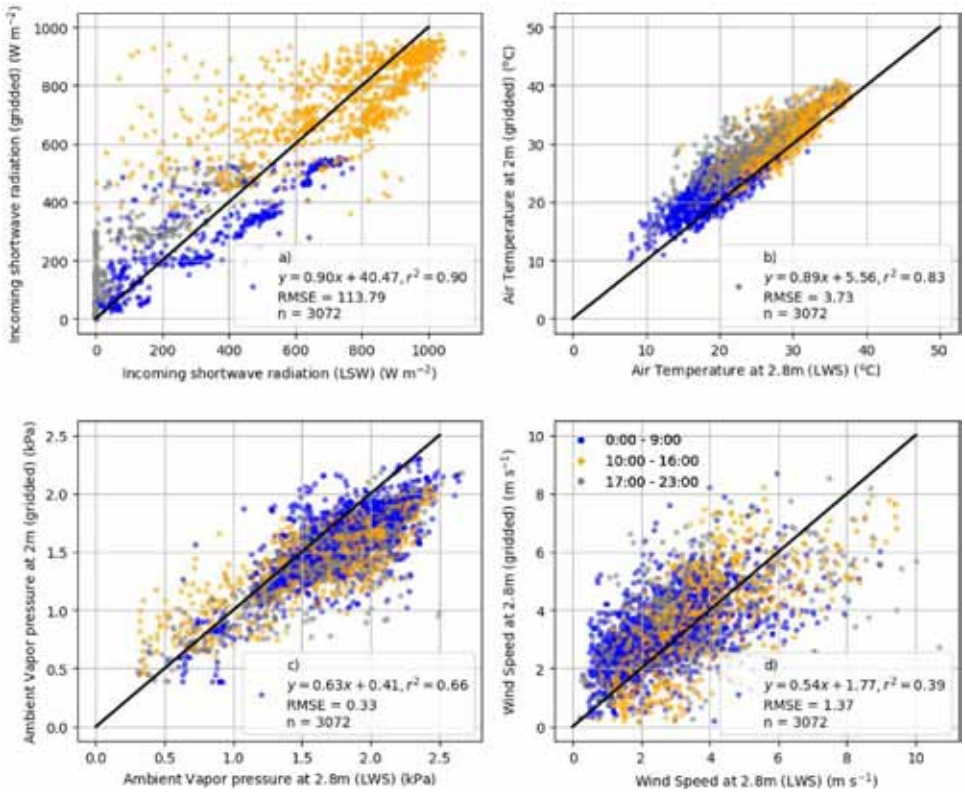

Fig. 3. Hourly scatterplots from local weather station (LWS) and gridded NLDAS a) incoming solar irradiance, b) air temperature, c) ambient vapor pressure, and d) wind speed between 22 May (DOY 143) and 26 September (DOY 270) 2016 at Bushland, Texas. Diel intervals (0:00–9:00, 10:00–16:00, 17:00–23:00) are indicated by symbol color; one-to-one correspondence (black line) as indicated.

2014). The u_z was more scattered than other parameters with some positive bias (Fig. 3d), where similar observations were found by (Luo et al., 2003; Lewis et al., 2014). The r^2 was 0.90, 0.83, 0.66, and 0.39 for $R_{s\downarrow}$, T_a, e_a, and u_z, respectively (Fig. 3). The computational difference between measured and gridded data may also have contributed some bias in e_a (Appendix A).

Comparison between Standard Weather Station (SWS) and Local Weather Station (LWS) Data

Figure 4 shows a comparison between weather data from the SWS and LWS. Regression of SWS data against LWS data resulted in an RMSE of 41.4 W m^{-2}, 0.76°C, 0.17 kPa, and 1.02 m s^{-1} and r^2 was 0.99, 0.99, 0.97, and 0.76, respectively for $R_{s\downarrow}$, T_a, e_a, and u_z. The u_z showed a larger variability (both underestimation and overestimation during the simulation period) especially overestimation after DOY 180 (Fig. 4d). The $R_{s\downarrow}$ (Fig. 4a) and e_a (Fig. 4c) at a standard weather station showed a minor systematic underestimation, while P (data not shown) showed a close match. The measurement heights, surface roughness, instrumentation biases, and microclimatic variations between these two sites may have contributed these variabilities. The u_z at SWS was measured at 2 m over irrigated fescue maintained at ~0.12 m height. However, u_z at the LWS was measured at corn field at 2.8 m above the soil surface. Therefore, as the corn crop grew, u_z measured height relative to the corn surface decreased from 2.8 m at planting to almost zero by tasseling. These differences in weather data may vary and possibly increase when the standard weather data is further away from the study site. SWS data is common and probably most adopted data source for both point and large-scale ET simulation, for instance using single SWS for the entire Landsat scene (190 km by 180 km).

Precipitation (P) and Irrigation (I_{rr})

Figure 5a shows daily P between LWS and NLDAS gridded data and Fig. 5b shows actual and simulated I_{rr}. We presented daily accumulated P and I_{rr} rather than hourly as there were larger variations and uncertainty in hourly values. Measured cumulative seasonal P was 225 mm while gridded was 286 mm. The P can have wide variations locally, especially in semiarid and arid climates. Uncertainty in gridded P data had been widely documented and is challenging meteorological variable (Adam and Lettenmaier, 2003; Xia et al., 2012; Abatzoglou, 2013). Applied I_{rr} was 491 mm while simulated was 616 mm. No I_{rr} was applied in the field after DOY 232 while model simulated I_{rr} through DOY 270, resulting in an overestimation of simulated I_{rr} (Fig. 5b). Simulated I_{rr} pattern and frequency showed slightly different behavior than applied I_{rr} (Fig. 5b). As this study was conducted for fully irrigated corn, I_{rr} pattern should have a minimal effect in ET as plant never gets stressed as per irrigation rules.

Vegetation Indices

Figure 6 shows that the calculated gridded LAI using Landsat (evaluated for a specific type of corn i.e., *Zea mays* L.) was systematically underestimated during full cover canopy (DOY 180 to 240). Measured LAI reached up to 5.5 m^2 m^{-2} around DOY 195 and remained 5.0 m^2 m^{-2} through DOY 240. However, the estimated gridded LAI was about 4.0 m^2 m^{-2} to 3.5 m^2 m^{-2} during the same period. Further evaluation of gridded LAI for various corn types, crops, and the adopted algorithm will help to understand if this specific behavior persists systematically. Underestimation of gridded LAI can create an asymmetry between f_c and LAI as they are closely related (Fig. 6a). The

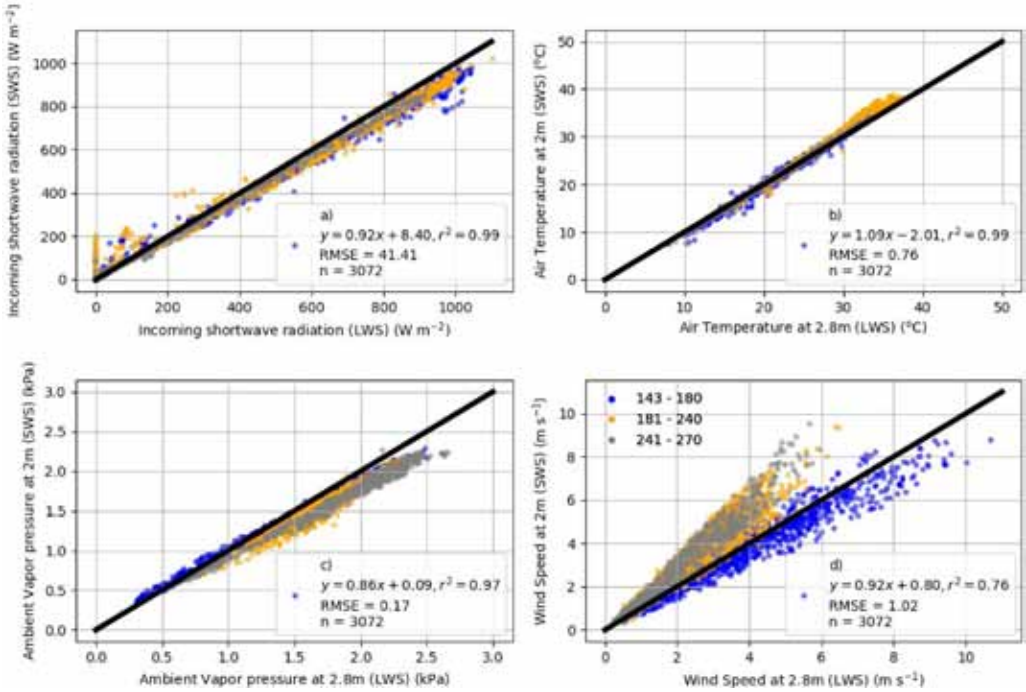

Fig. 4. Hourly scatterplots from local weather station (LWS) and standard weather station (SWS) a) incoming solar irradiance, b) air temperature, c) ambient vapor pressure, and d) wind speed between 22 May (DOY 143) and 26 September (DOY 270) 2016 at Bushland, Texas. DOYs (143–180, 181–240, 241–270) is indicated by symbol color; one-to-one correspondence (black line) as indicated.

f_c based on gridded *NDVI* closely followed f_c estimated from measured canopy width in the field. Gridded *LAI* and f_c both attended maximum values during full cover. The f_c value was ~ 0.9 during the full cover from both measured and estimated. Results indicated that linear interpolation of vegetation indices from Landsat based images was a reasonable option, though *LAI* showed a negative bias. Availability of Landsat based images during the start of growing season, full cover and senescence would help to reduce uncertainty in vegetation indices and increase the overall accuracy of seasonal *ET* calculation.

Influence of Gridded Data in ET

The influence and sensitivity of gridded meteorological data and Landsat based vegetation indices in *ET* (output at 30 m spatial resolution and hourly temporal resolution) was evaluated using BAITSSS in the coming sections (see Eq. [2a] and Table 2). Cumulative *ET* from lysimeter was 697 mm, from BAITSSS: 694 mm utilizing 15-min measured input weather data (Dhungel et al., 2018), 723 mm utilizing hourly averaged measured weather data (Table 2, scenario 'a'), 875 mm from all NLDAS gridded (scenario 'k'), and 789 mm from all gridded data (scenario 'l') for 127 d. Results indicated that the largest individual positive bias (deviations from measurements) occurred from $R_{s\downarrow}$ (+ 11%; Table 2, scenario 'f'), followed by q_a (+ 9%; Table 2, scenario 'e'), combined u_z and T_a (+ 8%; Table 2, scenario 'i'), and P (+ 4%, Table 2, scenario 'd') in cumulative *ET* when compared to the lysimeter.

We analyzed some of the reasons behind these biases based on model simulations (Eq. [2b]; scenario 'a' to other scenarios). Generally, increase in $R_{s\downarrow}$ (Table 2, scenario 'f') elevates the surface energy flux components and ultimately *ET*. For instance, on DOY 216 (12:00, r_{sc} = 40 s m^{-1}), $R_{s\downarrow}$ from measured was 404 W m^{-2} (scenario 'a') and from gridded 889 W m^{-2} (r_{sc} = 40 s m^{-1}; scenario 'f'), *ET* increased from 0.43 mm h^{-1} to 0.78 mm h^{-1} which accounts 79%. Similarly, on DOY 244 (13:00, r_{sc} = 40 s m^{-1}), $R_{s\downarrow}$ from measured was 217 W m^{-2} and from gridded 550 W m^{-2} (r_{sc} = 40 s m^{-1}), *ET* increased from 0.08 mm h^{-1} to 0.31 mm h^{-1} which accounts 287%. This difference in $R_{s\downarrow}$ explains 11% cumulative increase of *ET*.

The decrease in e_a (computed from q_a; Table 2, scenario 'e') increase VPD_s and VPD_c in Eq. [A-2a– A-2b] at the numerator that tended to increase both evaporation and transpiration. The decrease in e_a usually results in increased *VPD* for constant T_a. Furthermore, Eq. [A-17] shows a linear increase in r_{sc} with an increase in VPD_c due to smaller F_3 value. However, Eq. [A-2a–A-2b] show a proportional increase of LE_s and LE_c with an increase in *VPD*. This shows the complex relationship of *VPD* in BAITSSS based on the available literature. For instance, on DOY 194 (10:00 and $R_{s\downarrow}$ = 818 W m^{-2}, LAI = 5.6, r_{sc} = 40 s m^{-1}), e_a from measured was 2.26 kPa (scenario 'a') and from gridded 1.27 kPa (r_{sc} = 40 s m^{-1}; scenario 'f'), *ET* increased from 0.72 mm h^{-1} to 0.86 mm h^{-1} which accounts 19%. Similarly, DOY 218 (12:00 and $R_{s\downarrow}$ = 964 W m^{-2}, LAI = 5.4, r_{sc} = 40 s m^{-1}), e_a from measured was 2.3 kPa and from gridded 1.5 kPa (r_{sc} = 40 s m^{-1}), *ET* increased from 0.89 mm h^{-1} to 0.96 mm h^{-1} which accounts 8%.

Increase in u_z generally accelerates the turbulence process by decreasing r_{ah} in surface energy balance and ultimately increase *ET* (Hanson, 1991; Dhungel et al., 2016a). For instance, on DOY 236 (14:00 and $R_{s\downarrow}$ = 362 W m^{-2}, r_{sc} = 40 s m^{-1}), u_z from measured was 2.5 m s^{-1} (scenario 'a') and from gridded 7.02 m s^{-1} (r_{sc} = 40 s m^{-1}; scenario 'f'), *ET* increased from 0.5 mm h^{-1} to 0.73 mm h^{-1} which accounts 47%. Similarly, on DOY 203 (13:00 and $R_{s\downarrow}$ = 980 W m^{-2}, r_{sc} = 40 s m^{-1}), u_z from measured was 2.5 m s^{-1} and from gridded 5.2 m s^{-1} (r_{sc} = 40 s m^{-1}), *ET* increased from 1.05 mm h^{-1} to 1.2 mm h^{-1} which accounts 14%.

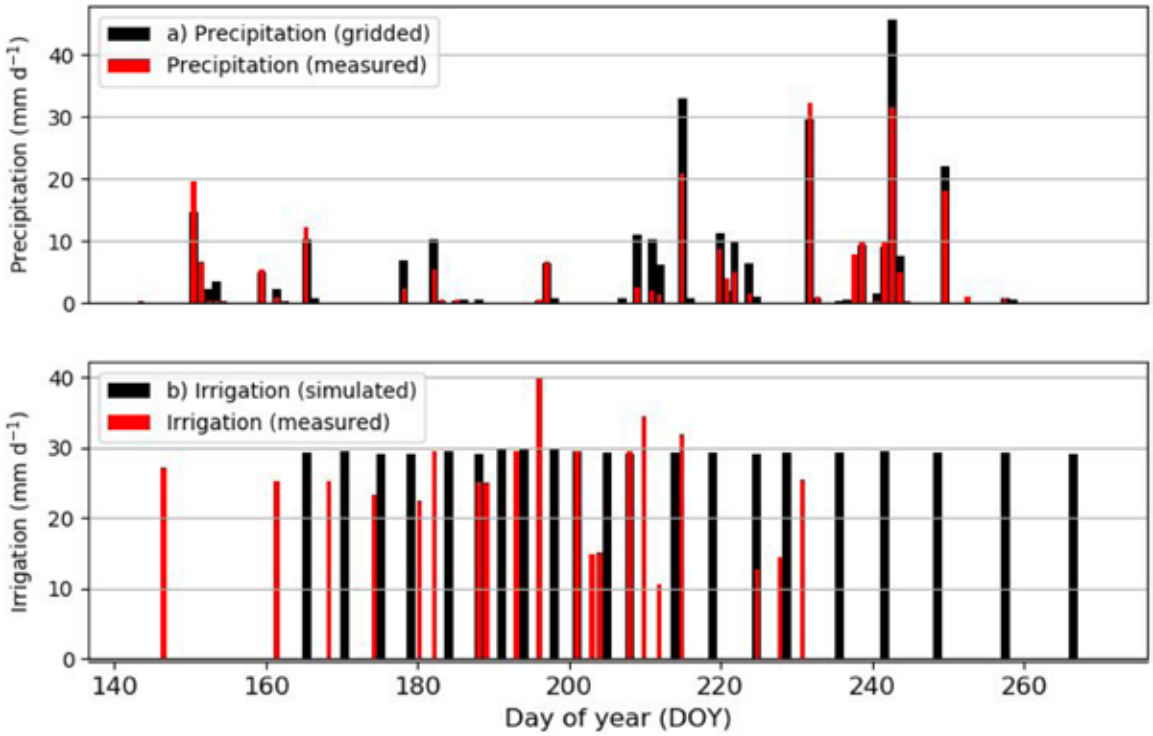

Fig. 5. Daily plots a) measured local weather station (LWS) and NLDAS gridded precipitation, b) measured and simulated irrigation between 22 May (DOY 143) and 26 September (DOY 270) 2016 at Bushland, Texas.

Implication of small *LAI* (scenario 'c') in full cover canopy at denominator is large r_{sc} (Eq. [A-13]) and decreased *ET* and vice versa. With identical R_{c_min} for irrigated croplands as suggested by Kumar et al., (2011) and identical meteorological data, significant player of *ET* variations in the 30 m grid is vegetation indices. Underestimation of *LAI* from gridded data may misrepresent vegetation types, though we assume that this underestimation may be systematic for all crop types. For instance, on DOY 207 (13:00 and $R_{s\downarrow}$ = 969 W m^{-2}), measured *LAI* was 5.6 m^2 m^{-2} (scenario 'a') and gridded LAI was 3.8 m^2 m^{-2} (scenario 'c'), *ET* decreased from 1.05 mm h^{-1} to 0.75 mm h^{-1} which account 28%. Simulated r_{sc} was 40 s m^{-1} from measured input (Table 2, scenario 'a') while 156 s m^{-1} from the gridded input (scenario 'c'). In other instances, when simulated r_{sc} were identical from both measured and gridded inputs (40 s m^{-1}), the results revealed a decrease in *ET* because of decreased *LAI* as it had also been used for calculating other variables like z_{om} and h_c. Finally, the variation in timing and frequency of *P* from NLDAS may have increased soil evaporation, which possibly contributed 5% positive bias in total *ET* (Table 2, scenario'd'). However, Table 2 scenario 'g', results indicated that there was no significant effect in *ET* because of mismatch in irrigation pattern for fully irrigated corn.

The individual biases from NLDAS weather data were substantial, therefore a combination of these accounted up to 25% bias with a resulting RMSE of 2 mm d^{-1} (scenario 'k'). In contrast, gridded *LAI* decreased cumulative *ET* by 5% (Table 2, scenario 'c'). *LAI*-induced uncertainty was 7% of total ET over the continental United States (Ferguson et al., 2010). Overall, the combination of gridded data (both weather data and vegetation indices) resulted in a 13% positive bias in cumulative *ET* (scenario 'l'). Results showed that uncertainty in input data had clearly propagated bias to final *ET*. Earlier studies that utilized NLDAS data reported similar positive bias in *ET* (Bhattarai et al., 2018). A positive bias in reference evapotranspiration (ET_o) computed from NLDAS data was reported (Abatzoglou, 2013). Similarly, Moorhead et al. (2015) found NOAA reference ET (ET_r) maps generally overestimated the TXHPET observations (1.4 and 2.2 mm d^{-1} ET_{os} and ET_{rs}, respectively) for Texas High Plains where they suspected uncertainty in the modeled NLDAS T_a and u_z.

Daily and Hourly ET

Figure 7 shows daily *ET* plots illustrating an agreement between lysimeter and model calculations for various gridded input and vegetation indices as shown in Table 2. The letters in figures are associated with letters (under column 'S.L.' with Scenarios) in Table 2. Figure 7a, 8a, and 9a (scenario 'a') show *ET* from hourly averaged input from 15-min measured observations without any gridded data. We evaluated this scenario (scenario 'a') to quantify the effect of temporal resolution on calculated *ET*, i.e., hourly from 15-min. The r^2 and RMSE were 0.90 and 0.85 mm for daily and 0.90 and 0.10 mm for hourly, respectively. Statistics showed a slight improvement in daily *ET* (r^2 and RMSE were 0.85 and 1.09 mm, respectively), reported for the daily time step in Dhungel et al. (2018) which used a 15-min time interval. This improved agreement was because of decreased initial soil water content at the surface i.e., 100 mm (reduced θ_{sur} from 0.15 to 0.05 m^3 m^{-3}) compared to the earlier study of the 15-min interval. However, there was a small increase (< 4%, earlier 694 mm) in cumulative *ET* with the hourly interval (Table 2, scenario 'a'). Revised R_{c_min} i.e., 150 s m^{-1} based on (Dhungel et al., 2018) during DOY 250 to 270 improved agreement between calculated and measured *ET* during the assumed senescence period.

Figure 8 and 9 show daily and hourly scatterplots of *ET*, respectively, between lysimeter and BAITSSS as in Table 2. Underestimation and overestimation of *ET* from various

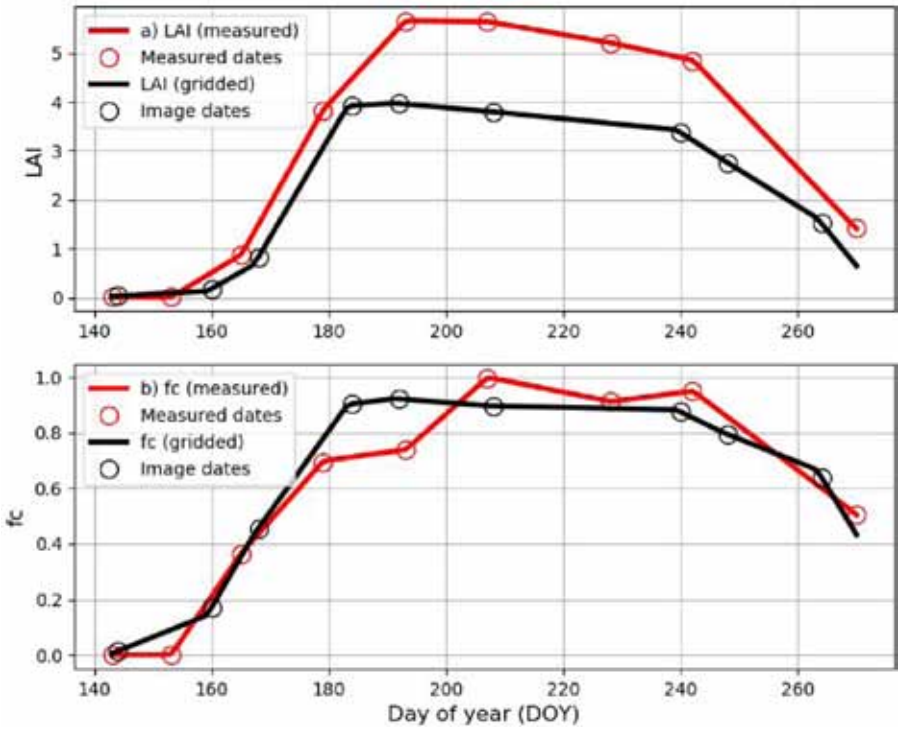

Fig. 6. a) Measured and gridded plots a) Leaf area index (*LAI*), b) fraction of canopy cover (f_c) of corn between 22 May (DOY 143) and 26 September (DOY 270) 2016 at Bushland, Texas. Measured dates and satellite acquisition dates are presented.

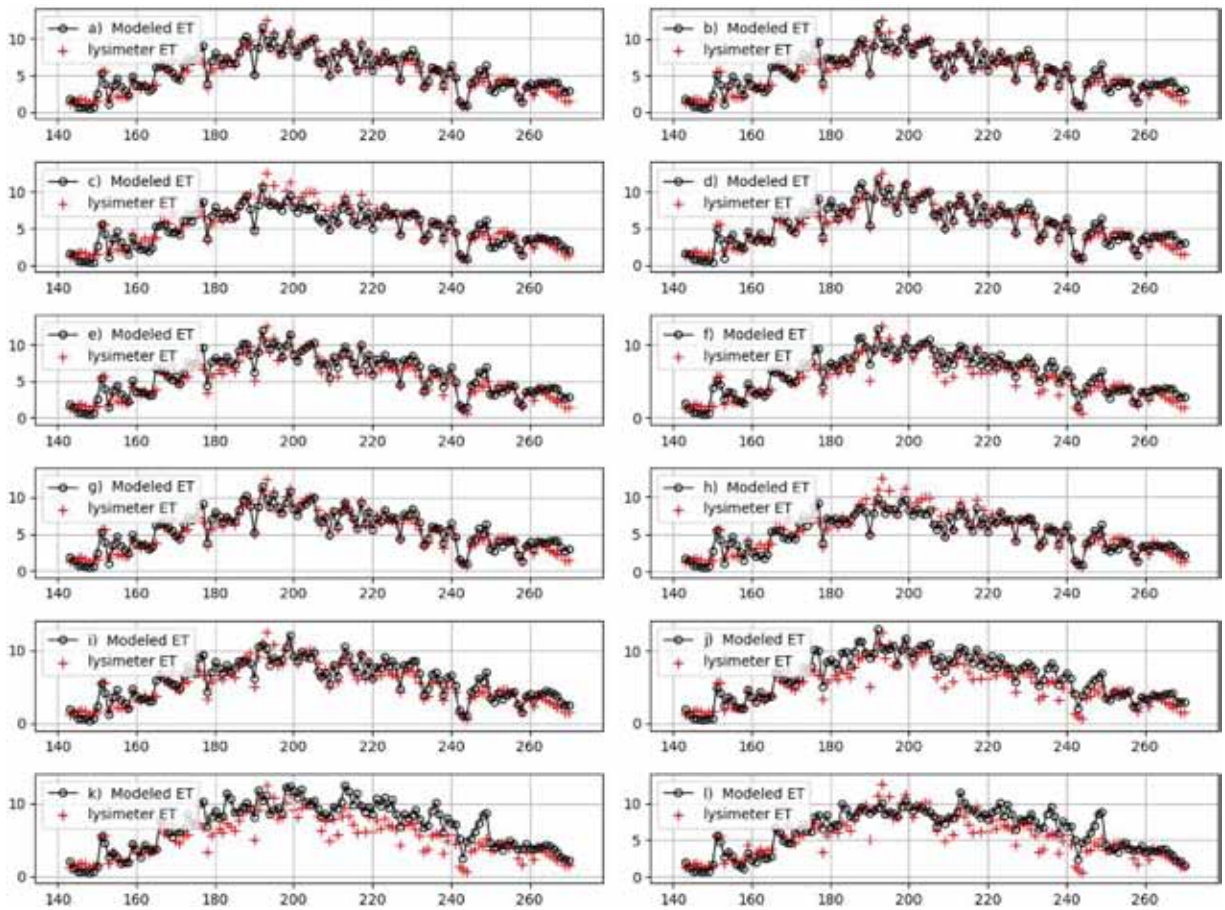

Fig. 7. Daily plots of *ET* from BAITSSS using various combinations of gridded and LWS measured data compared to lysimeter of corn between 22 May (DOY 143) and 26 September (DOY 270) 2016 at Bushland, Texas.

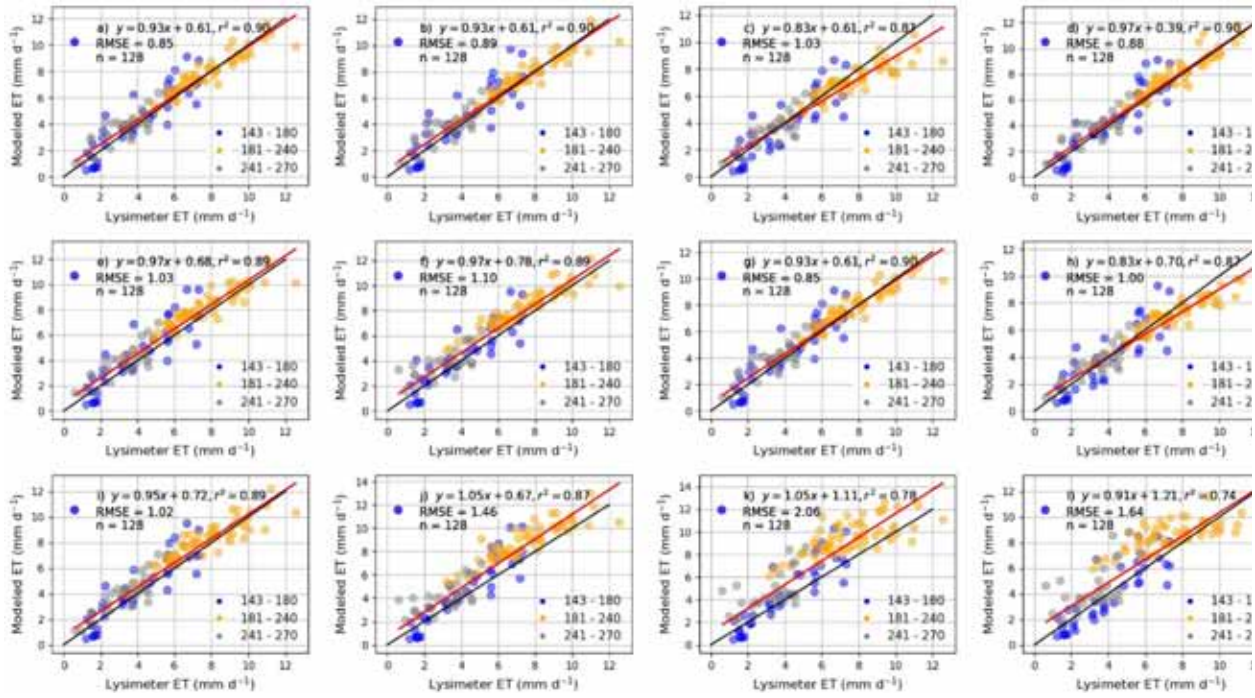

Fig. 8. Daily scatterplots of *ET* from BAITSSS using various combinations of gridded and LWS measured data compared to lysimeter of corn between 22 May (DOY 143) and 26 September (DOY 270) 2016 at Bushland, Texas. DOYs (143–180, 181–240, 241–270) are indicated by symbol color; linear regression (red lines) and one-to-one correspondence (black line) are indicated.

gridded data combinations were distinct in these scatterplots, especially during full cover canopy (DOY 180 – 240). Daily RMSE increased from 0.85 (Fig. 8a, all measured) to 1.64 mm (Fig. 8l, all gridded) with a maximum of 2.06 mm (Fig. 8k, all NLDAS). Similarly, hourly RMSE ranged from 0.10 mm (Fig. 9a, all measured) to 0.14 mm (Fig. 9l, all gridded) with a maximum of 0.16 mm (Fig. 9k, all NLDAS).

Surface Temperature and Net Radiation

In this section, we evaluate the competence of BAITSSS to compute the composite surface temperature (T_{com}; combined soil and canopy temperature) and composite net radiation (R_n; combined soil and canopy net radiation) based on the all measured data (scenario 'a', Fig. 10a and 10b). We documented differences based on the gridded data (scenario 'l', Fig. 10c and

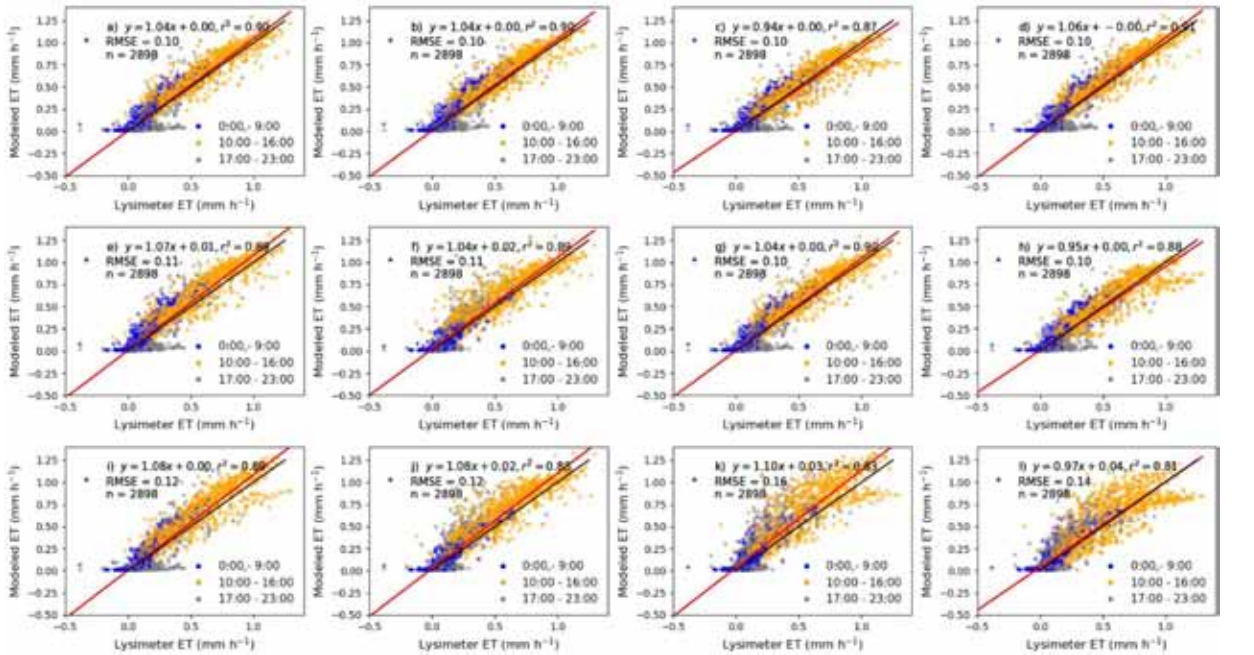

Fig. 9. Hourly scatterplots of *ET* from BAITSSS using various combinations of gridded and LWS measured data compared to lysimeter of corn between 22 May (DOY 143) and 26 September (DOY 270) 2016 at Bushland, Texas. Diel intervals (0:00–9:00, 10:00–16:00, 17:00–23:00) are indicated by symbol color; linear regression (red lines) and one-to-one correspondence (black line) are indicated.

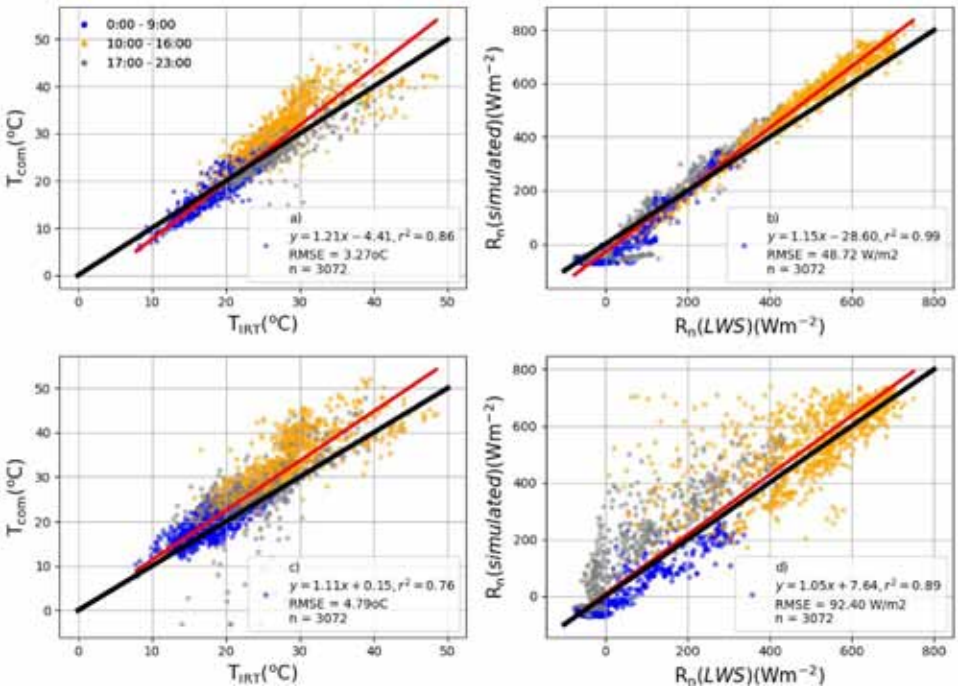

Fig. 10. Hourly scatterplots from BAITSSSS a) composite surface temperature (T_{com}), b) composite net radiation (R_n) from LWS measured data, c) T_{com}, and d) R_n from gridded data compared to IRT (T_{IRT}) and net radiometer of corn between 22 May (DOY 143) and 26 September (DOY 270) 2016 at Bushland, Texas. Diel intervals (0:00–9:00, 10:00–16:00, 17:00–23:00) are indicated by symbol color; linear regression (red lines) and one-to-one correspondence (black line) as also indicated.

10d). Comparison was performed with measured *IRT* and net radiometer. The r^2 and RMSE were 0.86 and 3.27°C for T_{com} and 0.99 and 49 W m^{-2} for R_n, respectively from measured inputs. However, the r^2 decreased and RMSE increased (0.76 and 4.79°C for T_{com} and 0.89 and 92 W m^{-2} for R_n) from gridded inputs indicating decreased accuracy. The propagation of bias in gridded inputs to T_{com} and R_n corresponds to the reduced accuracy of simulated *ET* (Table 2). Dhungel et al. (2018) discussed issues related to R_{c_min} in the Jarvis function, the possible role of local and regional advection, albedo, effective emissivity for incoming longwave irradiance calculation, and other unknown structural issues in BAITSSS, which may have contributed a positive bias in R_n and T_{com}. This positive bias tended to have minimal effect in *ET* (Fig. 7a, 8a, and 9a),

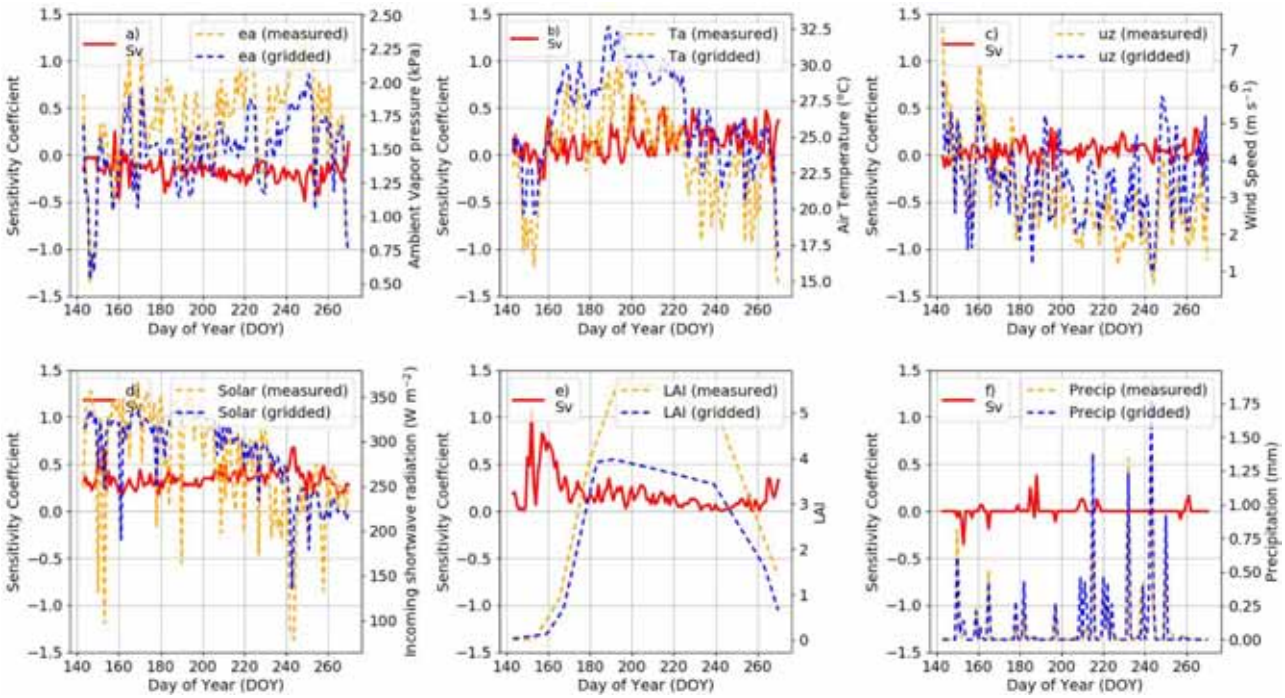

Fig. 11. Mean daily plots of sensitivity coefficients (*Sv*) and mean daily input data a) ambient vapor pressure, b) air temperature, c) wind speed, d) incoming solar irradiance, e) *LAI*, and f) precipitation between 22 May (DOY 143) and 26 September (DOY 270) 2016 at Bushland, Texas.

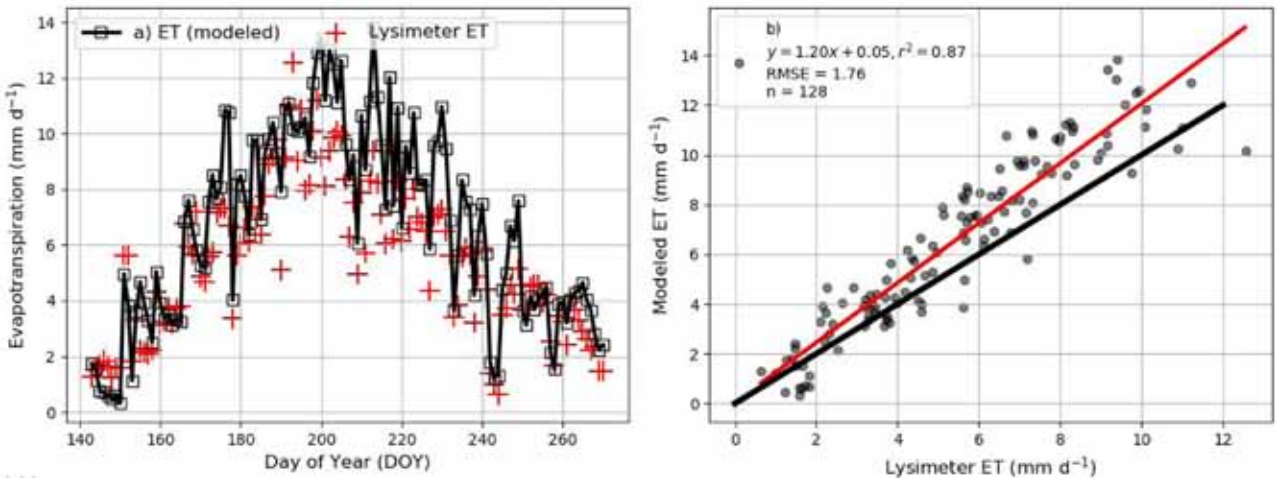

Fig. 12. Daily *ET* plots from BAITSSS using standard weather station (SWS) data and lysimeter a) time sequence b) scatterplot between 22 May (DOY 143) and 26 September (DOY 270) 2016 at Bushland, Texas. Linear regression (red lines) and one-to-one correspondence (black line) are indicated.

however, attempts to reduce T_{com} to match IRT subsequently increased *ET* (Dhungel et al., 2018).

Sensitivity Coefficients

Figure 11 shows daily mean sensitivity coefficients (S_v) in the primary vertical axis (Eq. [3]) and daily mean input data in the secondary vertical axis (LWS vs. gridded). The standard deviation (σ) of the variables in Eq. [3] were 0.42 kPa, 5.82°C, 1.61 m s^{-1}, 352.16 W m^{-2}, 1.98 m^2 m^{-2}, and 1.12 mm for e_a, T_a, u_z, $R_{s\downarrow}$, *LAI* and *P*, respectively. These S_v accounted for various random increase and decrease in input weather data based on the gridded data. Some large spike from outliers in sensitivity coefficients was restricted (shown in vertical axes limiting- 1.5 to + 1.5) before computing seasonal values. The daily sensitivity coefficients of input weather data and vegetation indices showed various forms, including changing signs (+ to– and vice versa) throughout the simulation. For instance, sensitivity coefficients of *LAI* were positive throughout the simulation because *LAI* difference was negative throughout the simulation (gridded smaller than measured) creating negative bias in *ET* (gridded *ET* smaller than actual, scenario 'c'). The mean seasonal (DOY 143 to 270) sensitivity coefficients were –0.16, 0.14, 0.04, 0.34, 0.18, 0.005 for e_a, T_a, u_z, $R_{s\downarrow}$, *LAI,* and *P* with largest seasonal S_v from $R_{s\downarrow}$. We confirmed that these sensitivity coefficients, especially seasonal values, can alter with adopted sensitivity equations (Ambas and Baltas, 2012), input data, and applied limits. These daily sensitivity coefficients were between –1.5 and +1.5 with seasonal sensitivities between –1 and +1.

Influence of Standard Weather Station (SWS) Data in ET

Earlier sections discussed the uncertainty and sensitivity of *ET* based on gridded data (NLDAS and remote sensing based vegetation indices) with LWS data. The extensive analysis based on gridded data will encompass the smaller degree of differences expected for SWS data, so we did not repeat the entire analysis using SWS data. In this section, we present *ET* from BAITSSS (Fig. 12) utilizing the widely available and adopted state of art type standard weather station (SWS) data (as of Fig. 4 and Table 1) and measured *LAI* and f_c from the ratio of width of canopy to row spacing. BAITSSS simulated cumulative *ET* from grass-referenced SWS data was 21% (cumulative *ET* of 843 mm) greater relative to lysimeter measured *ET* (increased RMSE = 1.76 mm and reduced r^2 = 0.87 for daily *ET*, Fig. 12a and 12b). These results were consistent with scenario 'k' of the simulation based on gridded NLDAS data input (overestimation of *ET* by 25% due to factors including larger u_z, warmer temperature, smaller e_a, and greater irradiance). Model simulation from BAITSSS indicated that even within close proximity (~ 250 m, Fig. 2), surprisingly the influence of weather data from SWS was pretty significant in *ET*. We further evaluated the bias in *ET* contributed especially by u_z which showed the largest variations among the SWS data (Fig. 4). The error in cumulative *ET* reduced to 10% when compared to lysimeter (771 mm) utilizing LWS u_z, keeping other variables as is from the SWS, indicating the major share in error. According to FAO-56 (Allen et al., 1998), u_z is measured at 10m for meteorological applications and 2 or 3 m for agrometeorological applications. The general circulation model (GCM) land surface scheme and some operational large scale *ET* models (Su, 2002; Anderson et al., 2005; Bastiaanssen et al., 2005; Allen et al., 2011a) extrapolate u_z to certain blending height (30 m – 200 m) to reduce the influence of surface roughness length, atmospheric stability, and heterogeneity length (Essery et al., 2003). Dhungel et al. (2016b) adopted a blending height of 30m for BAITSSS, where NCEP-NARR had weather data (T_a, u_z, and q_a) available in this height. However, the current study utilizes identical measurement height from the available data sources for both u_z and T_a (Table 1), i.e., LWS, SWS, and NLDAS without extrapolating u_z to the blending height. The source-specific measurement heights (momentum and heat) are incorporated in stability correction and aerodynamic resistance (r_{ah}) in these kinds of energy balance models (Appendix A for BAITSSS), differences in these measurement heights and its influence to *ET* probably warrants further evaluation and discussion. It also possibly indicates that some forms of bias may persist in *ET* modeling because of input weather variables if utilized without any adjustments (especially for u_z). However, further investigation of various sites and year probably guide us with a better understanding of this process and develop strategies to mitigate these kinds of biases.

CONCLUSION

We successfully automated BAITSSS model with NLDAS weather data and remote sensing based vegetation indices throughout the U.S. The BAITSSS model calculated hourly and daily *ET* (continuous 127 d) with $r^2 > 0.90$ (both hourly and daily) and RMSE of 0.1 mm (hourly) and 0.85 mm (daily), relative to lysimeter, when the site measured meteorological input (LWS) were used (less than 4% positive bias in cumulative *ET*). However, the calculated cumulative *ET* using NLDAS meteorological data was 25% larger compared to lysimeter measured *ET*. These discrepancies were related to NLDAS data having larger incoming $R_{s\downarrow}$, u_z, T_a, P, and smaller e_a compared with locally measured (LWS). Another caveat of these data sources was the difference in measurement height of wind (10 m for gridded, 2.8 m for LWS, and 2.0 m for SWS). The adopted *LAI* algorithm in the gridded data showed a negative bias during full cover canopy for this specific corn type. This bias partially compensated for the positive bias in *ET* due to NLDAS meteorological data. In general, the accuracy of f_c and *LAI* largely depends on the availability of images during phase changes such as growing, full cover and senescence, which influence the precision of seasonal *ET*. Propagation of bias based on sensitivity analysis in weather driving factors and vegetation indices from gridded data was −0.16, 0.14, 0.04, 0.34, 0.18, 0.005 for e_a, T_a, u_z, $R_{s\downarrow}$, *LAI,* and *P*, respectively.

BAITSSS simulation (i.e., based on its capability, adopted approach as well as structural limitations if any) indicated that weather data from SWS contributed 21% larger *ET* than lysimeter measured with RMSE of 1.76 mm d^{-1}. The significant error in *ET* from widely adopted SWS warrants further discussion to overcome these biases in operational *ET* models. Overall, weather data from the LWS (site specific) demonstrated superior to the rest of the data sets. However, it is not possible to have site specific data (like eddy covariance settings), so we have to rely on one of these available weather data sources. In addition, exploring a near weather station manually for each model run (either from LWS or SWS) will complicate the automation of *ET* models making gridded data as a viable option. The study indicated that both standard weather data and gridded may have relative advantages and disadvantages. It is critical to understand the uncertainty behind these input weather data and adopted adjustment procedure if any. With a more accurate and detailed modeling approach like BAITSSS, we can extend these kinds of analysis for multiple years and various sites to systematic quantification of these biases on a broader scale.

ACKNOWLEDGMENTS

Lysimeter and evapotranspiration research at USDA, Bushland, Texas were supported by USDA-ARS National Program 211, Water Availability and Watershed Management. This work was supported in part by the Ogallala Aquifer Program, a consortium of the USDA Agricultural Research Service, Kansas State University, Texas AgriLife Research, Texas AgriLife Extension Service, Texas Tech University, and West Texas A&M University. Numerous technicians and student workers contributed to the lysimeter and evapotranspiration programs. The water resource research group of Kimberly R & E, and Dr. Richard G. Allen, University of Idaho, is also acknowledged for various discussions related BAITSSS model during the code development phase.

APPENDIX A: BAITSSS MAJOR EQUATIONS (DHUNGEL ET AL., 2016B, 2018)

Surface energy balance equations of soil are represented by subscript *s* and canopy by subscript *c*. Latent heat flux (*LE*) and sensible heat flux (*H*) of soil and canopy surfaces are shown in Eq. [A-1– A-2], soil and canopy net radiation (R_{n_s} and R_{n_c}) in Eq. [A-5a–A-5b], respectively. Composite surface energy balance equations are shown in Eq. [A-7– A-10] (refer to Table A-1 for symbols).

Soil portion	Equation	Canopy portion	Equation
$H_s = \frac{\rho_a c_p (T_s - T_a)}{r_{ah} + r_{as}}$	[A-1a]	$H_c = \frac{\rho_a c_p (T_c - T_a)}{r_{ah} + r_{ac}}$	[A-1b]
$LE_s = \frac{C_p \rho_a}{\gamma}\left(\frac{e^o{}_s - e_a}{r_{as} + r_{ah} + r_{ss}}\right)$	[A-2a]	$LE_c = \frac{C_p \rho_a}{\gamma}\left(\frac{e^o{}_c - e_a}{r_{ac} + r_{ah} + r_{sc}}\right)$	[A-2b]
$G_s = \max(0.4 H_s, 0.15 R_{n\_s})$	[A-3]		
$R_{L\_s\uparrow} = T_s^4 \ \sigma \varepsilon_{o\_s}$	[A-4a]	$R_{L\_c\uparrow} = T_c^4 \ \sigma \varepsilon_{o\_c}$	[A-4b]
$R_{n\_s} = R_{s\downarrow} - \alpha_s R_{s\downarrow} + R_{L\downarrow} - R_{L\_s\uparrow} - (1 - \varepsilon_{o\_s}) R_{L\downarrow}$	[A-5a]	$R_{n\_c} = R_{s\downarrow} - \alpha_c R_{s\downarrow} + R_{L\downarrow} - R_{L\_c\uparrow} - (1 - \varepsilon_{o\_c}) R_{L\downarrow}$	[A-5b]
$H_s = R_{n\_s} - G_s - E_{ss} \lambda_s$	[A-6a]	$H_c = R_{n\_c} - T \lambda_c$	[A-6b]

Composite portion

$$H = H_c f_c + H_s (1 - f_c) \quad [A\text{-}7]$$

$$LE = LE_c f_c + LE_s (1 - f_c) \quad [A\text{-}8]$$

$$L = -\frac{c_p T_a \rho_a u.^3}{kgH} \quad [A\text{-}9]$$

$$r_{ah} = \frac{\left[\ln\left(\frac{z-d}{z_{om}}\right) - \psi_m\right]\left[\ln\left(\frac{z-d}{Z_1}\right) - \psi_h + \psi_h\left(\frac{Z_1}{L}\right)\right]}{k^2 u_z} \quad [A\text{-}10]$$

Roughness length of momentum (z_{om}) is computed based on *LAI* (Waters et al., 2002) (Eq. [A-11]).

$$z_{om} = 0.018\,LAI \quad \text{[A-11]}$$

Integration constant Z_1 (i.e., roughness length of heat (z_{oh}) for full cover vegetation; $f_c > 0.8$) is computed from Eq. [A-12]. For partial canopy ($f_c < 0.6$), it is computed based on height of canopy (h_c) and zero plane displacement (d). For intermediate canopy cover ($0.6 > f_c < 0.8$), Z_1 is weighted with fraction of canopy cover for smooth transition between partial and full.

$$z_{oh} = 0.1\,z_{om} \quad \text{[A-12]}$$

Constant albedo for soil (α_s) and canopy (α_c) is used as 0.2 and 0.15 (in Eq. [A-5a– A-5b]), respectively. Constant emissivity for both soil (ε_{o_s}) and canopy (ε_{o_c}) was 0.98 (Eq. [A-4a– A-4b, A-5a– A-5b]) throughout simulation.

Standard Jarvis type canopy resistance (r_{sc}; Eq. [A-13]), (Alfieri et al., 2008; Kumar et al., 2011) with weighting functions representing plant response to solar irradiance (F_1), air temperature (F_2), vapor pressure deficit (F_3), and soil water content (F_4) as per discussion (Dhungel et al., 2018).

$$r_{sc} = \frac{R_{c\_min}}{\frac{LAI}{f_c} F_1 F_2 F_3 F_4} \quad \text{[A-13]}$$

Effects of $R_{s\downarrow}$ were calculated (F_1, Eq. [A-14]) where R_{c_max} (5000 s m^{-1}) and R_{c_min} (40 s m^{-1} (Kumar et al., 2011) before assumed senescence, 150 s m^{-1} after assumed senescence) are maximum and minimum values of r_{sc} (s m^{-1}), respectively.

$$F_1 = \frac{\frac{R_{c\_min}}{R_{c\_max}} + f}{1 + f} \quad \text{[A-14]}$$

Parameter f of Eq. [A-14] is computed using Eq. [A-15] where $R_{S\downarrow\_min}$ (100 W m^{-2}) is assumed to be minimum $R_{s\downarrow}$ necessary for photosynthesis (Kumar et al., 2011).

$$f = 0.55 \frac{R_{S\downarrow}}{R_{S\downarrow\_min}} \left(\frac{2}{LAI}\right) \quad \text{[A-15]}$$

Temperature effects (F_2, Eq. [A-16]) were taken from Kumar et al. (2011).

$$F_2 = 1 - 0.0016\,(T_{ref} - T_a)^2 \quad \text{[A-16]}$$

where reference temperature (T_{ref}) is taken as 298 K and T_a is air temperature (K). Effects of VPD (F_3, Eq. [A-17]) were taken from Alfieri et al. (2008) as a linear relationship of vapor pressure deficit (VPD_c) where *VPD* is in kPa.

$$F_3 = 1 - 0.1914\,VPD_c \quad \text{[A-17]}$$

Canopy *VPD* ($VPD_c = e^o{}_c - e_a$) is computed based on saturated vapor pressure at canopy ($e^o{}_c = f(T_c)$) and ambient vapor pressure ($e_a = (RH/100)\,e_s$). Ambient *VPD* ($VPD_{amb} = e_s - e_a$) is computed based on saturated vapor pressure at ambient temperature [$e_s = f(T_a)$] and ambient vapor pressure (e_a). A logistic equation was used to calculate effects of available water fraction (*AWF*) (Eq. [A-18]) on F_4 [Eq. (A-19– A-20) (Anderson et al., 2007)].

$$AWF = \frac{\theta_{root} - \theta_{wp}}{\theta_{fc} - \theta_{wp}} \quad \text{[A-18]}$$

$$F_4 = \frac{ln(W)}{ln(W_f)} \quad \text{[A-19]}$$

$$W = \frac{W_0 W_f}{W_0 + (W_f - W_0) exp(-\mu\, AWF)} \quad \text{[A-20]}$$

where $W_o = 1$, $W_f = 800$, and $\mu = 12$.

A simplified formulation (Eq. [A-21]) (Sun, 1982) based on saturation soil water content (θ_{sat}) and soil water content at soil surface (θ_{sur}) are utilized to track soil surface resistance (r_{ss}).

$$r_{ss} = 3.5\left(\frac{\theta_{sat}}{\theta_{sur}}\right)^{2.3} + 33.5 \quad \text{[A-21]}$$

Water balance at soil surface (θ_{sur}) (100 mm) and root (θ_{root}) (100 mm- 2000 mm) is computed using Eq. [A-22– A–23], respectively as described by (Dhungel et al., 2016b).

$$\theta_{sur} = \theta_{sur(i-1)} + \frac{(P + I_{rr} - S_{run}) - E_{ss} - T_e}{d_{sur}} - DP_e + CR_e \quad \text{[A–22]}$$

where i is current time step, $\theta_{sur(i-1)}$ is volumetric water content (*VWC*) of surface layer for previous time steps, E_{ss} is soil surface evaporation, d_{sur} is soil surface depth, DP_e is deep percolated water from upper soil layer to root zone, CR_e is capillary rise from root zone into first soil surface (m^3 m^{-3}), and T_e is transpiration from soil surface layer (mm). CR_e and T_e are neglected to simplify soil water balance in this sub–model. Currently, model permits soil to be dry to an air-dry condition.

$$\theta_{root} = \theta_{root(i-1)} + \frac{(P + I_{rr} - S_{run}) - T - E_{ss}}{d_{root}} - DP + CR \quad \text{[A-23]}$$

where $\theta_{root(i-1)}$ is VWC of root zone from previous time steps, T is transpiration from vegetation, d_{root} is rooting depth, *DP* is deep percolation below root zone, and *CR* is capillary rise from third layer to root zone. Capillary rise (*CR*) from third layer into bulk layer (second) is also neglected.

Height of vegetation (h_c) is computed according to *LAI* suggested by Allen et al. (2012) (Eq. [A-24]).

$$h_c = 0.15\,LAI \quad \text{[A-24]}$$

Zero plane displacement (d) is computed from Eq. [A-25] (Choudhury and Monteith, 1988).

$$d = 1.1\,h_c\,\ln(1 + X^{\frac{1}{4}}) \quad \text{[A-25]}$$

where X is a parameter for calculating d. X parameter of zero-plane displacement is calculated using Eq. [A-26].

$$X = c_d\,LAI \quad \text{[A-26]}$$

where c_d is mean drag coefficient for individual leaves which is used as a 0.2 (Choudhury and Monteith, 1988). Attenuation

Table A-1 BAITSSS variables and imposed limits.

Variable	Symbol	Minimum	Maximum	Unit
Incoming solar irradiance	$R_{S\downarrow}$	–	–	W m^{-2}
Incoming longwave irradiance	$R_{L\downarrow}$	–	–	W m^{-2}
Net radiation	R_n	–	–	W m^{-2}
Net radiation of soil portion	R_{n_s}	–	–	W m^{-2}
Net radiation of canopy portion	R_{n_c}	–	–	W m^{-2}
Measurement height of wind speed and air temperature	z	–	–	m
Emissivity for soil portion	ε_{o_s}	–	–	–
Emissivity for canopy portion	ε_{o_c}	–	–	–
Atmospheric density	ρ_a	–	–	kg m^{-3}
Stability correction parameter	ψ	–	–	–
Specific heat capacity of moist air	c_p			J $(kg\ K)^{-1}$
Soil surface temperature	T_s	265	350	K
Canopy temperature	T_c	265	350	K
Air temperature	T_a	–	–	K
Wind speed	u_z	2.0	–	m s^{-1}
Relative humidity	RH	–	–	%
Soil surface evaporation	E_{ss}	0.0001	–	mm h^{-1}
Canopy transpiration	T	0.0001	–	mm h^{-1}
Composite (bulk) sensible heat flux	H	–200	500	W m^{-2}
Sensible heat flux for soil portion	H_s	–200	500	W m^{-2}
Sensible heat flux for canopy portion	H_c	–200	500	W m^{-2}
Ground heat flux	G	–200	200	W m^{-2}
Latent heat flux for soil	LE_s	–	–	W m^{-2}
Latent heat flux for canopy	LE_c	–	–	W m^{-2}
Latent heat of vaporization for soil portion	λ_s	–	–	J kg^{-1}
Latent heat of vaporization for vegetation portion	λ_c	–	–	J kg^{-1}
Saturation vapor pressure at the soil surface	e^o_s	–	–	kPa
Saturation vapor pressure at the canopy surface	e^o_c	–	–	kPa
Integration constant	Z_I	–	–	m
Actual vapor pressure of the air	e_a	–	–	kPa
Friction velocity	u^*	0.01	500	m s^{-1}
Aerodynamic resistance from canopy height to blending height	r_{ah}	1	500	s m^{-1}
Albedo soil	α_s	0.20	0.20	–
Albedo canopy	α_c	0.15	0.15	–
Leaf area index	LAI	–	–	m^2 m^{-2}
Fraction of canopy cover	f_c	0.05	1	–
Mean boundary layer resistance per unit area of vegetation	r_b	0	–	s m^{-1}
Roughness length of momentum	z_{om}	–	–	m
Roughness length of heat	z_{oh}	–	–	m
Minimum roughness length	z_{os}	0.01	–	m
Bulk boundary layer resistance of the vegetative elements in the canopy	r_{ac}	0	5000	s m^{-1}
Canopy resistance	r_{sc}	R_{c_min}	5000	s m^{-1}
Soil surface resistance	r_{ss}	35	5000	s m^{-1}
Aerodynamic resistance between the substrate and canopy height ($d + z_{om}$)	r_{as}	–	–	s m^{-1}
Height of canopy	h_c	–	–	m
Soil water content at surface	θ_{sur}	–	–	m^3 m^{-3}
Soil water content at root zone	θ_{root}	–	–	m^3 m^{-3}
Soil water content at wilting point	θ_{wp}	–	–	m^3 m^{-3}
Soil water content at field capacity	θ_{fc}	–	–	m^3 m^{-3}
Available water fraction	AWF	0	1	–

coefficient (n) is computed using Eq. [A-27] (Choudhury and Monteith, 1988)

$$n=\begin{cases} 2.5 \; if \; h_c<1m \\ 4.25 \; if \; h_c>10m \\ 2.31+0.194\,h_c \; Otherwise \end{cases} \quad [A\text{-}27]$$

When surface is fully covered with vegetation, understory aerodynamic resistance ($r_{as\,(fc=1)}$) between z_{os} and $d+z_{om}$ is computed as according to Choudhury and Monteith (1988) using Eq. [A-28].

$$r_{as(fc=1)}=\frac{h_c\,exp(n)}{n\,K(h)}\left[\exp\left(\frac{-n\,z_{om}}{h_c}\right)-\exp\left[-n\left[\frac{d+z_{om}}{h_c}\right]\right]\right] \quad [A\text{-}28]$$

The eddy diffusion coefficient of momentum correction ($K(h)$) from z_{om} to h_c has been computed using Eq. [A-29] (Choudhury and Monteith, 1988).

$$K(h)=\frac{k^2\,u_z\,(h_c-d)}{ln\left(\frac{z-d}{z_{om}}\right)-\psi_m} \quad [A\text{-}29]$$

where ψ_m is stability correction of momentum, z is height of measurements of wind speed. When surface is completely bare, aerodynamic resistance ($r_{as\,(fc=0)}$) from z_{os} to $d+z_{om}$ can be written using Eq. [A-30].

$$r_{as\,(fc=0)}=\frac{\left[\ln\left(\frac{z}{z_{os}}\right)-\psi_m\right]\left[\ln\left(\frac{d+z_{om}}{z_{os}}\right)-\psi_{h_d+zom}\right]}{k^2\,u_z} \quad [A\text{-}30]$$

Aerodynamic resistance for a partial surface $r_{as\,(int)}$ is computed weighting by f_c in a parallel combination of resistances (Eq. [A-31]).

$$r_{as\,(int)}=\frac{1}{\frac{f_c}{r_{as(f=1)}}+\frac{1-f_c}{r_{as(f=0)}}} \quad [A\text{-}31]$$

Bulk boundary layer resistance of vegetative elements (r_{ac}) is computed using Eq. [A-32].

$$r_{ac}=\frac{\frac{r_b}{2\,LAI}}{f_c} \quad [A\text{-}32]$$

where r_b is mean boundary layer resistance per unit area of vegetation. Aerodynamic resistance (r_{ah}) for fully vegetated and partially vegetated conditions is shown in Eq. [A-33].

$$r_{ah}=\begin{cases} \frac{\left[\ln\left(\frac{z-d}{z_{om}}\right)-\psi_m\right]\left[\ln\left(\frac{z-d}{z_{oh}}\right)-\psi_h\right]}{k^2\,u_z} \; if \; f_c=1 \\ \frac{\left[\ln\left(\frac{z-d}{z_{om}}\right)-\psi_m\right]\left[\ln\left(\frac{z-d}{h_c-d}\right)-\psi_h+\psi_{h(h_c-d)}\right]}{k^2\,u_z} \; Otherwise \end{cases} \quad [A\text{-}33]$$

Parameter X of stability correction for measurement height is computed from Eq. [A-34].

$$X=\left[1-16\frac{(z-d)}{L}\right]^{0.25} \quad [A\text{-}34]$$

Correction of momentum (ψ_m) for measurement height is computed from Eq. [A-35].

$$\psi_m=\begin{cases} 2\ln\left[\frac{(1+X)}{2}\right]+\ln\left[\frac{(1+X^2)}{2}\right]+2atanX-\frac{\pi}{2} \; if \; L<0 \\ -5\left(\frac{z}{L}\right) Otherwise \end{cases} \quad [A\text{-}35]$$

Correction of heat (ψ_h) for measurement height is computed from Eq. [A-36].

$$\psi_h=\begin{cases} 2\,ln\left(\frac{1+X^2}{2}\right) if \; L<0 \\ -5\left(\frac{z}{L}\right) Otherwise \end{cases} \quad [A\text{-}36]$$

Parameter X for $d+z_{om}$ is computed from Eq. [A-37].

$$X_{d+zom}=\left[1-16\frac{(d+Z_{om})}{L}\right]^{0.25} \quad [A\text{-}37]$$

Correction of heat for $d+z_{om}$ (Ψ_{hd+zom}) is computed from Eq. [A-38].

$$\psi_{h_d+zom}=\begin{cases} 2\,ln\left(\frac{1+X_{d+zom}{}^2}{2}\right) if \; L<0 \\ -5\left(\frac{d+Z_{om}}{L}\right) Otherwise \end{cases} \quad [A\text{-}38]$$

Parameter X for h_c-d is computed from Eq. A-39.

$$X_{h_c-d}=\left[1-16\frac{(h_c-d)}{L}\right]^{0.25} \quad [A\text{-}39]$$

Correction of heat for h_c-d ($\psi_{h(hc-d)}$) is computed from Eq. A-40.

$$\psi_{h(h_c-d)}=\begin{cases} 2ln\left(\frac{1+X_{h_c-d}{}^2}{2}\right) if \; L<0 \\ -5\left(\frac{h_c}{L}\right) Otherwise \end{cases} \quad [A\text{-}40]$$

REFERENCES

Abatzoglou, J.T. 2013. Development of gridded surface meteorological data for ecological applications and modelling. Int. J. Climatol. 33(1):121–131. doi:10.1002/joc.3413

Adam, J.C., and D.P. Lettenmaier. 2003. Adjustment of global gridded precipitation for systematic bias. J. Geophys. Res. Atmos. 108(D9). doi:10.1029/2002JD002499

Alfieri, J.G., D. Niyogi, P.D. Blanken, F. Chen, M.A. LeMone, K.E. Mitchell, M.B. Ek, and A. Kumar. 2008. Estimation of the minimum canopy resistance for croplands and grasslands using data from the 2002 International H2O Project. Mon. Weather Rev. 136(11):4452–4469. doi:10.1175/2008MWR2524.1

Allen, R., A. Irmak, R. Trezza, J.M. Hendrickx, W. Bastiaanssen, and J. Kjaersgaard. 2011a. Satellite-based ET estimation in agriculture using SEBAL and METRIC. Hydrol. Processes 25(26):4011–4027. doi:10.1002/hyp.8408

Allen, R.G., L.S. Pereira, T.A. Howell, and M.E. Jensen. 2011b. Evapotranspiration information reporting: I. Factors governing measurement accuracy. Agric. Water Manage. 98(6):899–920. doi:10.1016/j.agwat.2010.12.015

Allen, R.G., L.S. Pereira, D. Raes, and M. Smith. 1998. FAO Irrigation and drainage paper No. 56. Rome Food Agric. Organ. U. N. 56(97):E156.

Allen, R.G., R. Trezza, M. Tasumi, and J. Kjaersgaard. 2012. Mapping evapotranspiration at high resolution using internalized calibration: Application manual for Landsat satellite imagery. University of Idaho. Version 2.0, 2012.

Ambas, V.T., and E. Baltas. 2012. Sensitivity analysis of different evapotranspiration methods using a new sensitivity coefficient. Glob. NEST J. 14(3):335–343.

Ampas, V. 2010. Research and estimation of meteorological parameters with direct impact on agriculture. Ph.D. Thesis. Aristotle University of Thessaloniki, Greece.

Anderson, M.C., R.G. Allen, A. Morse, and W.P. Kustas. 2012. Use of Landsat thermal imagery in monitoring evapotranspiration and managing water resources. Remote Sens. Environ. 122:50–65. doi:10.1016/j.rse.2011.08.025

Anderson, M.C., J.M. Norman, W.P. Kustas, F. Li, J.H. Prueger, and J.R. Mecikalski. 2005. Effects of vegetation clumping on two–source model estimates of surface energy fluxes from an agricultural landscape during SMACEX. J. Hydrometeorol. 6(6):892–909. doi:10.1175/JHM465.1

Anderson, M.C., J.M. Norman, J.R. Mecikalski, J.A. Otkin, and W.P. Kustas. 2007. A climatological study of evapotranspiration and moisture stress across the continental United States based on thermal remote sensing: 1. Model formulation. J. Geophys. Res. Atmos. 112(D10). doi:10.1029/2006JD007506

Bastiaanssen, W.G.M., E.J.M. Noordman, H. Pelgrum, G. Davids, B.P. Thoreson, and R.G. Allen. 2005. SEBAL model with remotely sensed data to improve water-resources management under actual field conditions. J. Irrig. Drain. Eng. 131(1):85–93. doi:10.1061/(ASCE)0733-9437(2005)131:1(85)

Beven, K. 1979. A sensitivity analysis of the Penman-Monteith actual evapotranspiration estimates. J. Hydrol. 44(3–4):169–190. doi:10.1016/0022-1694(79)90130-6

Bhattarai, N., K. Mallick, N.A. Brunsell, G. Sun, and M. Jain. 2018. Regional evapotranspiration from an image-based implementation of the Surface Temperature Initiated Closure (STIC1.2) model and its validation across an aridity gradient in the conterminous US. Hydrol. Earth Syst. Sci. 22(4):2311–2341. doi:10.5194/hess-22-2311-2018

Brutsaert, W.H. 1982. Evaporation into the atmosphere: Theory, history, and applications. D. Reidel Publishing Co. Dordrecht. doi:10.1007/978-94-017-1497-6

Choudhury, B.J., and J.L. Monteith. 1988. A four-layer model for the heat budget of homogeneous land surfaces. Q. J. R. Meteorol. Soc. 114(480):373–398. doi:10.1002/qj.49711448006

Courault, D., B. Seguin, and A. Olioso. 2005. Review on estimation of evapotranspiration from remote sensing data: From empirical to numerical modeling approaches. Irrig. Drain. Syst. 19(3–4):223–249. doi:10.1007/s10795-005-5186-0

Dhungel, R., R.M. Aiken, P.D. Colaizzi, R.L. Baumhardt, D. Brauer et al. 2018. Evaluation of the uncalibrated energy balance model (BAITSSS) for estimating evapotranspiration in a semiarid, advective climate. In review, Rev. Hydrol. Process.

Dhungel, R., R.G. Allen, and R. Trezza. 2016a. Improving iterative surface energy balance convergence for remote sensing based flux calculation. J. Appl. Remote Sens. 10(2):026033. doi:10.1117/1.JRS.10.026033

Dhungel, R., R.G. Allen, R. Trezza, and C.W. Robison. 2016b. Evapotranspiration between satellite overpasses: Methodology and case study in agricultural dominant semi-arid areas. Meteorol. Appl. 23(4):714–730. doi:10.1002/met.1596

Essery, R.L.H., M.J. Best, R.A. Betts, P.M. Cox, and C.M. Taylor. 2003. Explicit representation of subgrid heterogeneity in a GCM land surface scheme. J. Hydrometeorol. 4(3):530–543. doi:10.1175/1525-7541(2003)004<0530:EROSHI>2.0.CO;2

Evett, S.R., T.A. Howell, A.D. Schneider, K.S. Copeland, D.A. Dusek, D.K. Brauer, J.A. Tolk, G.W. Marek, T.M. Marek, and P.H. Gowda. 2016. The Bushland weighing lysimeters: A quarter century of crop ET investigations to advance sustainable irrigation. Trans. ASABE 59(1):163–179. doi:10.13031/trans.59.11159

Ferguson, C.R., J. Sheffield, E.F. Wood, and H. Gao. 2010. Quantifying uncertainty in a remote sensing-based estimate of evapotranspiration over continental USA. Int. J. Remote Sens. 31(14):3821–3865. doi:10.1080/01431161.2010.483490

Gong, L., C. Xu, D. Chen, S. Halldin, and Y.D. Chen. 2006. Sensitivity of the Penman–Monteith reference evapotranspiration to key climatic variables in the Changjiang (Yangtze River) basin. J. Hydrol. 329(3–4):620–629. doi:10.1016/j.jhydrol.2006.03.027

Gowda, P.H., J.L. Chavez, P.D. Colaizzi, S.R. Evett, T.A. Howell, and J.A. Tolk. 2008. ET mapping for agricultural water management: Present status and challenges. Irrig. Sci. 26(3):223–237. doi:10.1007/s00271-007-0088-6

Guo, D., S. Westra, and H.R. Maier. 2017. Sensitivity of potential evapotranspiration to changes in climate variables for different Australian climatic zones. Hydrol. Earth Syst. Sci. 21(4):2107–2126. doi:10.5194/hess-21-2107-2017

Hanson, R.L. 1991. Evapotranspiration and droughts. U.S. Geol. Surv. Water Supply Pap. 2375:99–104.

Khanal, S., J. Fulton, and S. Shearer. 2017. An overview of current and potential applications of thermal remote sensing in precision agriculture. Comput. Electron. Agric. 139:22–32. doi:10.1016/j.compag.2017.05.001

Kiptala, J., M. Mul, Y. Mohamed, W. Bastiaanssen, and P. van der Zaag. 2018. Mapping Ecological Production and Benefits from Water Consumed in Agricultural and Natural Landscapes: A Case Study of the Pangani Basin. Remote Sens. 10(11):1802.

Kotlarski, S., A. Block, U. Böhm, D. Jacob, K. Keuler, R. Knoche, D. Rechid, and A. Walter. 2005. Regional climate model simulations as input for hydrological applications: Evaluation of uncertainties. Adv. Geosci. 5:119–125. doi:10.5194/adgeo-5-119-2005

Kumar, A., F. Chen, D. Niyogi, J.G. Alfieri, M. Ek, and K. Mitchell. 2011. Evaluation of a photosynthesis-based canopy resistance formulation in the Noah land-surface model. Bound.-. Layer Meteorol. 138(2):263–284. doi:10.1007/s10546-010-9559-z

Lewis, C.S., H.M. Geli, and C.M. Neale. 2014. Comparison of the NLDAS Weather Forcing Model to Agrometeorological Measurements in the western United States. J. Hydrol. 510:385–392. doi:10.1016/j.jhydrol.2013.12.040

Luo, L., A. Robock, K.E. Mitchell, P.R. Houser, E.F. Wood, J.C. Schaake, D. Lohmann, B. Cosgrove, F. Wen, J. Sheffield, Q. Duan, R.W. Higgins, R.T. Pinker, and J.D. Tarpley. 2003. Validation of the North American land data assimilation system (NLDAS) retrospective forcing over the southern Great Plains. J. Geophys. Res. Atmos. 108(D22). doi:10.1029/2002JD003246

Mitchell, K.E., D. Lohmann, P.R. Houser, E.F. Wood, J.C. Schaake, A. Robock, B.A. Cosgrove, J. Sheffield, Q. Duan, L. Luo, R.W. Higgins, R.T. Pinker, J.D. Tarpley, D.P. Lettenmaier, C.H. Marshall, J.K. Entin, M. Pan, W. Shi, V. Koren, J. Meng, B.H. Ramsay, and A.A. Bailey. 2004. The multi-institution North American Land Data Assimilation System (NLDAS): Utilizing multiple GCIP products and partners in a continental distributed hydrological modeling system. J. Geophys. Res. Atmos. 109(D7). doi:10.1029/2003JD003823

Moorhead, J., P. Gowda, M. Hobbins, G. Senay, G. Paul, T. Marek, and D. Porter. 2015. Accuracy assessment of NOAA gridded daily reference evapotranspiration for the Texas High Plains. JAWRA J. Am. Water Resour. Assoc. 51(5):1262–1271.

Petropoulos, G., P. Srivastava, M. Piles, and S. Pearson. 2018. Earth observation-based operational estimation of soil moisture and evapotranspiration for agricultural crops in support of sustainable water management. Sustainability 10(1):181. doi:10.3390/su10010181

Renard, B., D. Kavetski, G. Kuczera, M. Thyer, and S.W. Franks. 2010. Understanding predictive uncertainty in hydrologic modeling: The challenge of identifying input and structural errors. Water Resour. Res. 46(5). doi:10.1029/2009WR008328

Root, T.L., and S.H. Schneider. 2002. Strategic cyclical scaling: Bridging five orders of magnitude scale gaps in climatic and ecological studies. Integrated Assess. 3(2–3):188–200. doi:10.1076/iaij.3.2.188.13573

Saxton, K.E. 1975. Sensitivity analyses of the combination evapotranspiration equation. Agric. Meteorol. 15(3):343–353. doi:10.1016/0002-1571(75)90031-X

Schimel, D.S., V. Participants, and B.H. Braswell. 1997. Continental scale variability in ecosystem processes: Models, data, and the role of disturbance. Ecol. Monogr. 67(2):251–271. doi:10.1890/0012-9615(1997)067[0251:CSVIEP]2.0.CO;2

Su, Z. 2002. The Surface Energy Balance System (SEBS) for estimation of turbulent heat fluxes. Hydrol. Earth Syst. Sci. 6(1):85–100. doi:10.5194/hess-6-85-2002

Sun. 1982. Moisture and Heat Transport in a Soil Layer Forced by Atmospheric Conditions. M.S. Thesis, Department of Civil Engineering, University of Connecticut, U.S.A.

Von Schuckmann, K., M.D. Palmer, K.E. Trenberth, A. Cazenave, D. Chambers, N. Champollion, J. Hansen, S.A. Josey, N. Loeb, P.-P. Mathieu, B. Meyssignac, and M. Wild. 2016. An imperative to monitor Earth's energy imbalance. Nat. Clim. Chang. 6(2):138–144. doi:10.1038/nclimate2876

Wang, S., M. Pan, Q. Mu, X. Shi, J. Mao, C. Brümmer, R.S. Jassal, P. Krishnan, J. Li, and T.A. Black. 2015. Comparing evapotranspiration from eddy covariance measurements, water budgets, remote sensing, and land surface models over Canada. J. Hydrometeorol. 16(4):1540–1560. doi:10.1175/JHM-D-14-0189.1

Waters, R., R. Allen, W. Bastiaanssen, M. Tasumi, and R. Trezza. 2002. SEBAL. Surf. Energy Balance Algorithms Land Ida. Implement. Adv. Train. Users Man. Ida. USA. Python. 2018. Python.org. https://www.python.org/ (accessed 28 Dec. 2018).

Woolway, R.I., I.D. Jones, D.P. Hamilton, S.C. Maberly, K. Muraoka, J.S. Read, R.L. Smyth, and L.A. Winslow. 2015. Automated calculation of surface energy fluxes with high-frequency lake buoy data. Environ. Model. Softw. 70:191–198. doi:10.1016/j.envsoft.2015.04.013

Xia, Y., K. Mitchell, M. Ek, B. Cosgrove, J. Sheffield, B. Cosgrove, E. Wood, L. Luo, C. Alonge, H. Wei, J. Meng, B. Livneh, D. Lettenmaier, V. Koren, Q. Duan, K. Mo, Y. Fan, and D. Mocko. 2012. Continental-scale water and energy flux analysis and validation for North American Land Data Assimilation System project phase 2 (NLDAS-2): 2. Validation of model-simulated streamflow. J. Geophys. Res. Atmos. 117(D3).